Received: 19 June 2021 | Revised: 9 May 2022 | Accepted: 2 June 2022

DOI: 10.1002/nag.3412

RESEARCH ARTICLE

WILEY

Phase transition in monodisperse granular materials: How to model it by using a strain hardening visco-elastic-plastic constitutive relationship

Pietro Marveggio[1] | **Irene Redaelli**[2] | **Claudio di Prisco**[1]

[1]Department of Civil and Environmental Engineering, Politecnico di Milano, Milan, Italy

[2]Department of Architecture, Built Environment, and Construction Engineering, Politecnico di Milano, Milan, Italy

Correspondence
Pietro Marveggio, Department of Civil and Environmental Engineering, Politecnico di Milano, Piazza Leonardo da Vinci 32, 20133 Milan, Italy.
Email: pietro.marveggio@polimi.it

Abstract

During heating (loading characterised by a progressive increase in strain rate) and cooling (loading characterised by a progressive decrease in strain rate) numerical tests, performed by using Discrete Element codes, granular materials experience phase transition phenomena, named in this paper 'dry liquefaction' (when from solid the material starts behaving like a fluid) and 'dry resolidification' (freezing, when the material from fluid starts behaving like a solid). The aim of this paper consists in reproducing phase transition phenomena by using a strain hardening visco-elastic-plastic model based on the critical state concept and kinetic theories of granular gases. The authors demonstrate that crucial is the role of isotropic softening/hardening, which describes the size of the elastic domain and the capability of the solid skeleton of storing elastic energy according to permanent force chains. The main ingredients of the model are: (i) the additivity of quasi-static and collisional stresses, (ii) the energy balance equation governing the evolution of the granular temperature, interpreted this latter as an additional internal variable for the system for the collisional contribution, (iii) the mixed isotropic and kinematic hardening characterising the quasi-static incremental constitutive relationship. The model has been both calibrated and validated on Discrete Element Method (DEM) numerical results, obtained by testing dry assemblies of monodisperse spheres under true triaxial loading conditions.

KEYWORDS
constitutive modelling, phase transitions, strain rate dependence

1 | INTRODUCTION

As is well known, in nature, granular media behave differently according to their state: for instance, under quasi-static conditions, a sand deposit under a raft foundation behaves like a solid and can be idealised as a network of permanent force chains developing among grains.[1,2] In contrast, when flowing at large values of strain rate, the same material exhibits a fluid-like behaviour with grains colliding among each other.[3–5]

An attempt to experimentally investigate the mechanical behaviour of granular material in a wide range of strain rates is in Yamamuro et al.[6] This unique series of experimental results was obtained by means of an unconventional triaxial apparatus. These results put in evidence that an increase in shear rate corresponds to an increase in (i) stiffness at small strains, (ii) residual shear strength and (iii) dilatancy. These preliminary results testify the role of both strain rate and strain acceleration in affecting the mechanical behaviour of granular soils, but the study conducted by the authors was not systematic and did not investigate the response when the loading process is arrested.

In case of ideal materials, in the last 20 years, in the physicists community, numerous Discrete Element Method (DEM) numerical simulation results[7,8] have confirmed the role of both strain rate and confining pressure in governing the mechanical behaviour of granular media. DEM results are extremely useful when fundamental research is performed, since they provide microstructural information (for instance contact forces, energetic contributions and microstructure),[9] nowadays also partially available owing to the use of sophisticated experimental devices.[10,11] DEM can be used as an effective numerical tool, capable of capturing many inherent aspects of the soil response, although they do not directly account for many peculiarities of the soil behaviour related to grain shape, crushing, damage and indentation.[1,12–14]

In the scientific literature, very few[15–17] are the models capable of dealing with phase transition phenomena. In fact, the very numerous standard geotechnical constitutive models, introduced in the last five decades, based on elastic-plasticity,[18,19] on bounding surface plasticity,[20] on hypoplasticity[21,22] or incrementally non-linear formulations,[23] are capable of successfully predicting the material response under quasi-static conditions but are not adequate for simulating granular media in both the previously mentioned regimes; whereas, in the hydraulics/physicists community, popular are the theories/approaches proposed to describe the mechanical behaviour of granular media under fluid-like conditions. These, based on either experimental tests or numerical data, consider steady conditions only, disregard the micromechanics governing the phenomena and do not take into account phase transition processes.[4,24–26] To this category of models belongs the so called μ–I rheology,[4] according to which, under simple shear conditions, a unique relationship between stress level μ, void ratio e and inertial number I exists: high values of I correspond to agitated conditions, whereas small I values to quasi-static regimes. The unicity of such relationship, in case of deformable spheres, has been recently critically discussed by Redaelli and di Prisco[27,28] and Marveggio et al.[29]

The challenging goal of this paper consists in introducing a constitutive approach capable of reproducing phase transition phenomena ('dry liquefaction', when from solid the material starts behaving like a fluid, and 'freezing' or 'dry resolidification', when the material from fluid starts behaving like a solid) experienced by granular assemblies when either confining pressure is nullified/increased or strain rate is increased/decreased. The proposed model considers transient conditions and is based on the comprehension of the dissipative and storing mechanisms governing the phenomena and on the hypothesis of distinguishing collisional dissipation contributions from the ones related to long elapsing force chains. For steady conditions, the model follows the approach proposed in Berzi et al.,[30] Vescovi et al.[31] and Redaelli and di Prisco,[27] where a parallel scheme is adopted to account for separately both quasi static (i.e., force chains related) and collisional terms. The former contribution is evaluated by employing the so-called critical state theory,[32] whereas the latter one according to the kinetic theories of granular gases.[33–36] Recently, the same approach has been extended by Vescovi et al.[37] to account saturated conditions for. The same framework has been employed to simulate transient dry simple shear conditions by Redaelli et al.,[38] in which the quasi-static contribution is computed according to the standard elastic perfectly plastic theory, modified by including the critical state concept. This model could reproduce solid to fluid like transition process but not the vice versa. Thus, it has been modified by introducing a kinematic hardening[39] and validated against DEM simulation results to reproduce liquefaction and post-liquefaction response under isochoric conditions. The model seems to be capable of reproducing DEM results but not the nullification of the material history after liquefaction.

In this paper, a strain hardening visco-elastic-plastic model is proposed to overcome all the limitations mentioned here above. The model is based on the assumption that the evolution of the isotropic hardening variable (measuring the capability of the solid skeleton of storing elastic energy by means of permanent force chains) has to follow the one of the coordination number, whereas the back stress hardening rule, the one of the second invariant of the deviator of fabric tensor. When solid to fluid phase transition occurs, the material memory is assumed to be partially delated, since the isotropic hardening variable is assumed to experience a severe softening, whereas the second invariant of the back-stress is assumed not to evolve. During the reconsolidation process, the material is assumed to behave like a 'pseudo-virgin' material, characterised by an initial not negligible induced (from the previous strain history) anisotropy. In the model proposed in this paper (i) a 3D formulation is adopted, (ii) a closed shaped yield surface is employed, (iii) a mixed isotropic-kinematic strain hardening, based on critical state theory for granular materials,[40] via the definition of a back-stress tensor is introduced

and (iv) in agreement with what put in evidence by DEM numerical data of Huang et al.[41] but not considered by popular critical state based constitutive models like those previously cited,[19,42] the dependence of both critical void ratio and critical obliquity on Lode angle is accounted for. The constitutive model is validated against the numerical results obtained by Redaelli and di Prisco,[28] by discussing phase transition in terms of evolution of stored energy (elastic and fluctuating kinetic), stresses and internal variables.

In Section 2, by analysing DEM simulation data available in literature, the concept of phase transition is clarified. In Section 3, the constitutive model is introduced, while in Section 4 a constitutive parameters calibration procedure is described. Then, the model is validated against DEM 'heating' (i.e., monotonic loading during which the strain rate is increased) test results (Subsection 5.1). The role of (i) initial void ratio, (ii) Lode angle (from pure compression to extension) and (iii) deviatoric strain rate is accounted for. In Subsection 5.2, 'cooling' triaxial test (performed on specimens initially sheared under steady conditions by progressively decreasing the strain rate) results are discussed. Finally, the model is employed to predict the state of stress at rest after performing cycles of heating and cooling, performed at different acceleration/deceleration values (Subsection 5.3).

2 | NUMERICAL EVIDENCE OF PHASE TRANSITIONS IN GRANULAR MEDIA

According to Jop et al.,[4] under steady conditions, solid and fluid-like regimes can be distinguished as a function of inertial number I, since only in the solid-like regime stress ratio μ and void ratio e do not depend on I.

On the contrary, Redaelli and di Prisco[27] by performing DEM triaxial compression tests have shown that, at steady state, for sufficiently small inertial number values, the relationship between e and I is not unique as the void ratio seems to be independent of the deviatoric imposed strain rate $\dot{J}_e$ but markedly decreases with the imposed confining pressure $I_{1\sigma}$.

They have proposed three regimes: the solid (quasi static), the transitional and the fluid-like (collisional[35]) one (Figure 1). As is evident, only in the transitional regime both stress level and void ratio remain constant with I.

Under evolving conditions, Redaelli and di Prisco[28] have analysed DEM results of constant pressure (dashed lines HP, starting from initial condition I1) and constant volume (solid lines HV, starting from initial condition I2) triaxial compression tests (Figure 2), performed by imposing different deviatoric strain rates. By focusing on both stored energy and coordination number Z, they have individuated a condition identifying the boundary from transitional to collisional regimes and vice versa: the passage through lines $Z = Z_{\mathrm{T}}$ and $\frac{E_{el}}{E_{kf}} = 1$, where E_{el} is valued as the elastic energy stored at the contacts (durable and collisional), while E_{kf} is defined as the kinetic fluctuating energy.

The dotted line is the locus obtained by interpolating the steady state points (HI with $I = 1,..,6$) of the triaxial tests. As is evident, the intersection between the two straight lines previously mentioned belongs to this locus.

3 | THEORETICAL MODEL

The model, inspired to the numerical observation previously outlined, is defined by assuming the parallel scheme proposed by the authors in the above-mentioned papers. The stress tensor $\boldsymbol{\sigma}$ is thus defined as:

$$\boldsymbol{\sigma} = \boldsymbol{\sigma}^{qs} + \boldsymbol{\sigma}^{col}, \tag{1}$$

where the quasi-static solid skeleton contribution, $\boldsymbol{\sigma}^{qs}$, refers to the contact network, whereas the collisional one, $\boldsymbol{\sigma}^{col}$, is associated with collisions among particles. Once the quasi-static contribution is incrementally formulated, if an Euler explicit time integration scheme is adopted, the constitutive relationship can be written as follows[38]:

$$\boldsymbol{\sigma}_i = \left(\boldsymbol{D}^{qs}_{i-1}\Delta t + \mathbf{H}^{col}_{i-1}\right) : \dot{\boldsymbol{\varepsilon}}_i + \boldsymbol{\sigma}^{qs}_{i-1} + \boldsymbol{h}^{col}_{i-1}, \tag{2}$$

where symbol : stands for double scalar product, 'dot over' stands for the time derivative, while subscript i for the i-th integration time step. $\boldsymbol{\varepsilon}$ is the strain tensor, $\mathbf{H}^{col}_{i-1}$ and $\boldsymbol{D}^{\mathrm{qs}}_{i-1}$ the viscous collisional (Subsection 3.1) and the quasi-static tangent stiffness 4th order tensors (Subsection 3.2), respectively, evaluated at the (i−1)-th time step, Δt is the time step employed in the explicit time integration, $\boldsymbol{\sigma}^{qs}_{i-1}$ the quasi-static stress tensor evaluated at the previous integration time step and $\boldsymbol{h}^{col}_{i-1}$ is a collisional-related term (Subsection 3.1).

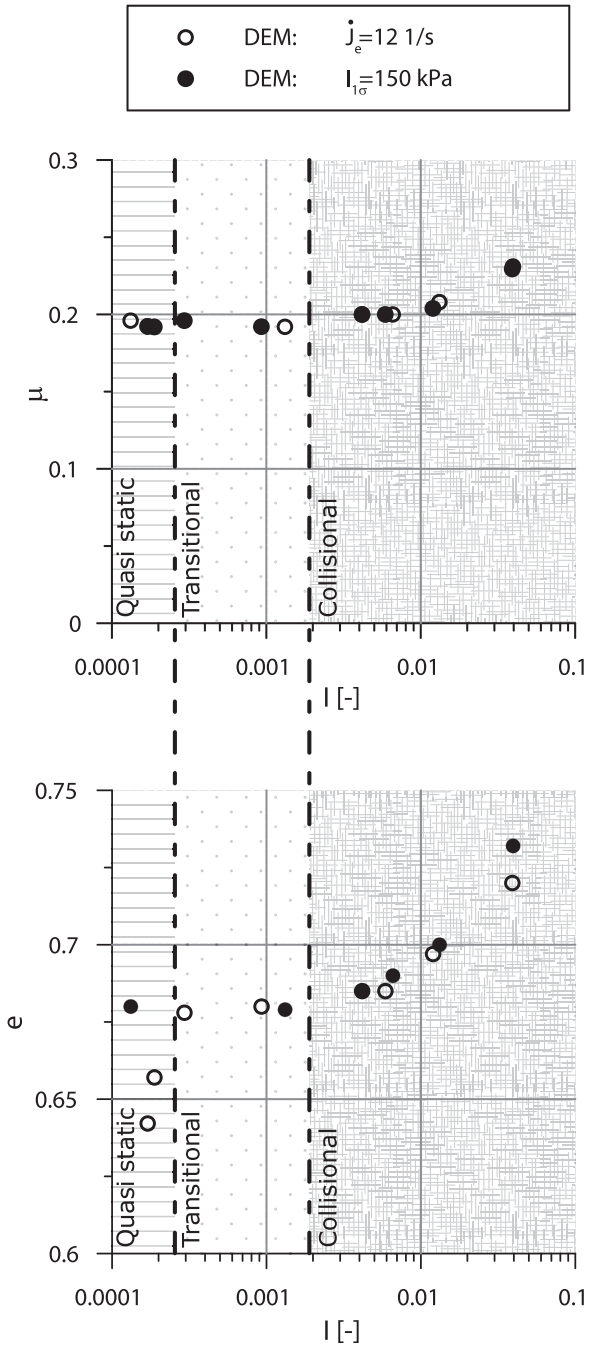

FIGURE 1 Steady state points of discrete element method (DEM) triaxial compression tests (A) inertial number – stress ratio plane, (B) inertial number – void ratio plane. Empty data points are characterised by the same deviatoric strain rate ($\dot{J}_e = 121/s$) and different confining pressures ($I_{1\sigma}$), filled data points are characterised by the same confining pressure ($I_{1\sigma} = 150$ kPa) and different deviatoric strain rates ($\dot{J}_e$). Data from Redaelli and di Prisco[27]

3.1 | Collisional contribution

As in Redaelli and di Prisco,[27] the collisional contribution is modelled according to kinetic theories of granular gases.[33–36] This approach assumes as state variables both void ratio e and granular temperature T, where this latter measures the system agitation and is defined as one third of the grain velocity variance.[33]

The evolution laws for both e and T are given in Subsection 3.1.1, while the collisional stress definition, in terms of the two viscous collisional tensors $\mathbf{H}^{col}$ and $\boldsymbol{h}^{col}$, is introduced in Subsection 3.1.2.

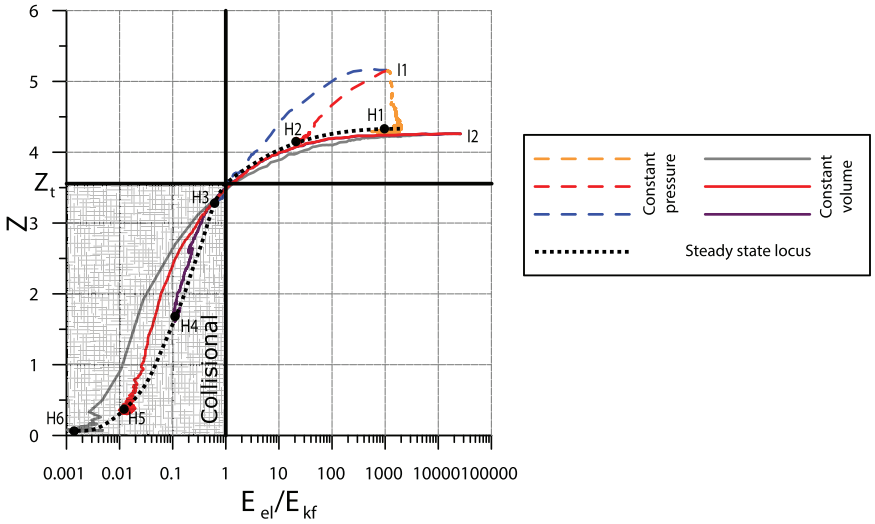

FIGURE 2 Phase diagram, in terms of stored energy ratio (elastic over kinetic fluctuating) and coordination number Z, under evolving conditions (solid lines) and steady limit (dotted line). HP tests are those under constant pressure (dashed line), HV under constant volume (solid line). Data from Redaelli and di Prisco[28]

3.1.1 | e and T evolution laws

Void ratio evolution law is governed by the mass balance, as it follows:

$$\dot{e} = -(1+e)\,\mathrm{Tr}(\boldsymbol{\varepsilon}), \tag{3}$$

whereas the evolution of granular temperature is ruled by the fluctuating energy E_f balance[30]:

$$\dot{E}_f = \boldsymbol{\sigma}^{col} : \dot{\boldsymbol{\varepsilon}} - \Gamma^{col}. \tag{4}$$

As in Vescovi et al.,[39] Γ^{col} is the rate of energy dissipated by inelastic collisions, given by[73]:

$$\Gamma^{col} = \frac{\rho_p}{L} F_4 T^{\frac{3}{2}}. \tag{5}$$

where ρ_p is the particle density, F_4 is a function of both e and T and its expression, is discussed in Subsection 3.1.2null . L, whose expression is reported in Appendix B, is the so-called correlation length, representing the size of particle clusters developing in the collisional regime.

In contrast, the novelty introduced in this paper consists in accounting for the elastic energy stored by the system during collisions ($E_{f,el}$) as a function of the fluctuating kinetic energy ($E_{f,k}$):

$$E_f = E_{f,k} + E_{f,el}, \tag{6}$$

where, according to Garzò and Dufty[34]:

$$E_{f,k} = \frac{3}{2}\rho_p \frac{1}{1+e} T, \tag{7}$$

whereas, according to the authors:

$$E_{f,el} = \frac{3}{2}\rho_p \frac{1}{1+e} T f_r(T,e), \tag{8}$$

being f_r (Appendix B) calculated, according to Berzi and Jenkins,[43] as the ratio of collision duration and flight time (i.e., average time elapsing between two subsequent collisions). In Equation (8), the average elastic energy stored during each collision is evaluated equal to the fluctuating kinetic energy. As in Berzi and Jenkins,[43] f_r accounts for the collision frequency in a representative elementary volume (REV), depending on T and e. According to these definitions, when

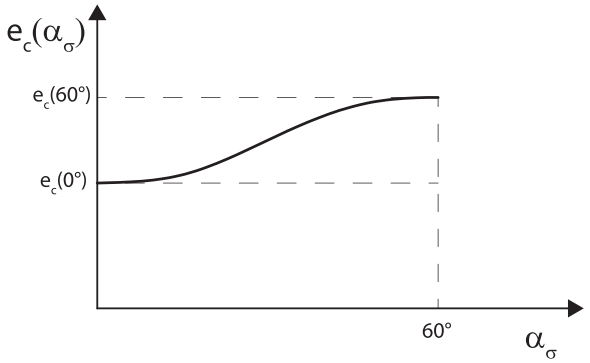

FIGURE 3 Jamming void ratio: Lode angle dependence

no stable force chains are present in the system and the grain flight time is negligible with respect to particle collision duration, $f_r = 1$ and the energy is equally stored in terms of kinetic fluctuations and elastic potential energy.

3.1.2 | Collisional stress

As in Redaelli et al.,[38] viscous collisional tensors $\mathbf{H}^{col}$ and $\boldsymbol{h}^{col}$ are defined as:

$$\mathbf{H}^{col} = \mathrm{H}^{col}_{ijkl} = \begin{cases} \rho_P d \left(\frac{4}{3}F_2 + F_3\right) T^{\frac{1}{2}} & \text{if } i = j = k = l \\ \rho_P d \left(-\frac{2}{3}F_2 + F_3\right) T^{\frac{1}{2}} & \text{if } i = j \cap k = l \cap i \neq k \\ \rho_P d F_2 T^{\frac{1}{2}} & \text{if } i \neq j \ \cap i = k \cap j = l \\ 0 & \text{elsewhere} \end{cases} \tag{9}$$

and

$$\mathbf{h}^{col} = \rho_P F_1 T \boldsymbol{I}, \tag{10}$$

being I the 2nd order identity tensor, F_1, F_2 and F_3 three functions of e and T (Equation 11) and d the particle diameter.

$F_i, i = 1, \ldots, 4$ (where F_4 is required to define the rate collisional dissipation in Subsection 3.1.1) are defined to take the particle deformability into account, according to Berzi and Jenkins[43]:

$$F_i = \begin{cases} \frac{\tilde{f}_i}{\rho_p^{1/2} T^{1/2}} \left(\frac{\tilde{f}_i}{f_i \rho_p^{1/2} T^{1/2}} + 1 \right)^{-1} & \text{if } e < e_c(\alpha_\sigma) \\ \frac{\tilde{f}_i}{\rho_p^{1/2} T^{1/2}} & \text{if } e > e_c(\alpha_\sigma) \end{cases}, \tag{11}$$

being f_i and $\tilde{f}_i$, $i = 1,\ldots,4$ only functions of void ratio (Appendix B), depending on one macroparameter (e_m) and three input data (particle Young modulus E_p, interparticle friction coefficient μ_p and restitution coefficient ε_n). e_c is the jamming void ratio, that is the void ratio at which force chains start developing within the granular medium under steady conditions. According to Zhao and Guo,[44] Zhou et al.[45] and Redaelli and di Prisco,[27] e_c is independent of the loading path. In contrast, Barreto and O'Sullivan[46] and Huang et al.[41] have numerically shown that e_c depends on Lode angle $\alpha_\sigma = \mathrm{atan}[\frac{\sqrt{3}(\sigma_y - \sigma_z)}{2\sigma_x - \sigma_y - \sigma_z}]$ (being σ_x, σ_y and σ_z the maximum, intermediate and minimum, respectively, principal stresses). In particular, the maximum value of jamming void ratio is expected in case of extension, while the minimum for compression. For this reason, the authors introduce for e_c the following expression (Figure 3):

$$e_c(\alpha_\sigma) = \frac{1}{2}\left[(e_{cc} + e_{ce}) + (e_{cc} - e_{ce})\cos 3\alpha_\sigma\right], \tag{12}$$

where e_{cc} and e_{ce} are the values of critical void ratio associated with compression and extension loading paths, respectively.

3.2 | Quasi-static contribution

The quasi-static contribution is modelled by employing a time independent elastic-plastic anisotropic strain hardening formulation, based on the critical state theory, interpreted this latter as a limit steady state for T going to zero.[27] According to elastic-plasticity, stiffness tensor $\boldsymbol{D}^{qs}$ of Equation (2) is assumed to coincide with the elastic stiffness tensor $\boldsymbol{D}^{el}$ (Subsection 3.2.1) under unloading, whereas under loading:

$$\boldsymbol{D}^{qs} = \boldsymbol{D}^{el} - \frac{\boldsymbol{D}^{el} : \boldsymbol{n} \otimes \frac{df}{d\boldsymbol{\sigma}^{qs}} : \boldsymbol{D}^{el}}{\frac{df}{d\boldsymbol{\sigma}^{qs}} : \boldsymbol{D}^{el} : \boldsymbol{n} + H}, \tag{13}$$

where $\otimes$ stands for tensor product, f the yield function (Subsection 3.2.2), $\boldsymbol{n}$ a second order tensor governing the plastic strain rate direction (Subsection 3.2.3) and H the hardening modulus (Subsection 3.2.4), this latter defined as:

$$H = -\sum_{1}^{\bar{N}} \frac{df}{dq_i} \left(\frac{dq_i}{d\varepsilon^{pl}} : \boldsymbol{n} \right), \tag{14}$$

being q_i the i-esim out of $\bar{N}$ model hardening variable.

3.2.1 | Elastic stiffness tensor

A hyperelastic formulation with non-nil elastic stiffness, when elastic strains nullify, is mandatory to reproduce the material mechanical behaviour at the solid-to-fluid transition. Since defining an expression for the elastic potential satisfying these requirements is a non-trivial operation and is out of the scope of this paper, for the sake of simplicity, the elastic contribution is modelled as linear and isotropic: elastic plastic coupling due to both void ratio dependence and elastic stiffness tensor anisotropy are disregarded.[47,48] The elastic stiffness tensor $\boldsymbol{D}^{el}$ is thus assumed to be constant and only a function of Young modulus E and Poisson ratio ν.

3.2.2 | Yield function

A closed shaped yield locus is employed: this choice, as will be discussed in Section 5, is fundamental for correctly simulating phase transition processes. The authors adopted the expression proposed in the model of di Prisco et al.[49]:

$$f = 3\beta\,(\gamma - 3)\ln\left(\frac{r}{r_c}\right) + \frac{9}{4}(\gamma - 1)J^*_{2\sigma} - \gamma J^*_{3\sigma}, \tag{15}$$

where γ is a dimensionless constitutive parameter, while:

$$r = \boldsymbol{\sigma}^{qs} : \boldsymbol{\chi}, \tag{16}$$

$$J^*_{2\sigma} = 3\boldsymbol{s}^{qs*} : \boldsymbol{s}^{qs*}/r^2, \tag{17}$$

$$J^*_{3\sigma} = 9\sqrt{3}det(\boldsymbol{s}^{qs*})/r^3, \tag{18}$$

$$\boldsymbol{s}^{qs*} = \boldsymbol{\sigma}^{qs} - r\boldsymbol{\chi}. \tag{19}$$

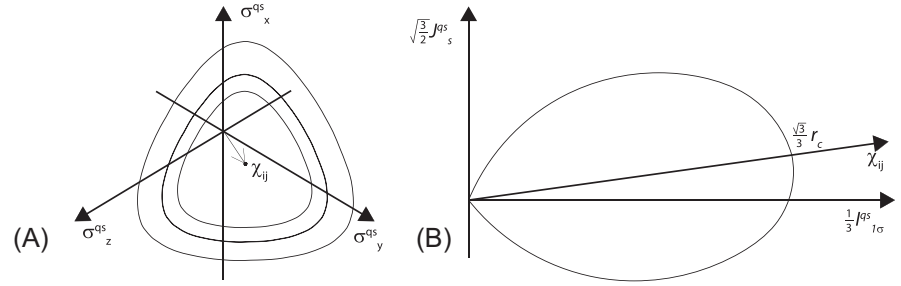

FIGURE 4 Yield surface in (A) deviatoric and (B) meridian planes. The geometrical role of the back-stress and the cap size is clarified in (B)

As is clarified in Figure 4, $\boldsymbol{\chi}$ is a back-stress second order tensor evolving with plastic strains, whereas r_c, equivalent to the isotropic pre-consolidation pressure for an isotropic material, defines the size of yield locus f. β controls, instead, the yield locus shape. In the original model, all these quantities vary with plastic strains. For the sake of simplicity and since an ideal material is considered in this paper, β is assumed to be a constant constitutive parameter.

3.2.3 | Flow rule

According to Manzari and Dafalias[42] and Vescovi et al.,[39] the direction of the plastic strain rate tensor $\dot{\boldsymbol{\varepsilon}}^p$ in the triaxial plane may be assumed to be ruled by a function F_d, depending on both void ratio and stress level. As was suggested by Manzari and Dafalias,[42] in the model proposed by the authors, the flow rule is assumed to be associated in the deviatoric plane and not associated in the meridian one. Therefore $\boldsymbol{n}$ (Equation 13) is written as:

$$\boldsymbol{n} = \sqrt{\frac{3}{2}} \frac{\frac{df}{d\boldsymbol{s}^{qs}}}{\left|\frac{df}{d\boldsymbol{s}^{qs}}\right|} + \frac{1}{3} F_d\left(\boldsymbol{\sigma}^{qs}, e\right) \boldsymbol{I}. \tag{20}$$

where $\boldsymbol{s}^{qs} = \boldsymbol{\sigma}^{qs} - \frac{1}{3} I_{1\sigma}^{qs} \boldsymbol{I}$ is the deviatoric stress, with $I_{1\sigma}^{qs} = Tr\left(\boldsymbol{\sigma}^{qs}\right)$, whereas F_d is defined by generalising to 3D loading paths the expression proposed for simple shear conditions by Vescovi et al.[39]:

$$F_d\left(\boldsymbol{\sigma}^{qs}, e\right) = \delta_1 \Psi\left(\boldsymbol{\sigma}^{qs}, e\right) + \delta_2 \Phi\left(\boldsymbol{\sigma}^{qs}\right) \tag{21}$$

being δ_1 and δ_2 two constant parameters.

In Equation (21), Ψ is a generalised version of the state variable introduced by Been et al.[50] and Jefferies.[40] In fact, as was mentioned in the introduction, the critical state void ratio for $I_{1\sigma}^{qs} \to 0$ axis is given by Equation (12). Therefore, by linearising the dependence of critical state locus on $I_{1\sigma}^{qs}$, as suggested by both Vescovi et al.[39] and 3D-DEM numerical data, obtained for steady simple shear flows of monodisperse spherical particles by Sun and Sundaresan[8]:

$$\Psi = e - e_c\left(\alpha_\sigma\right) + \frac{2}{3aE_p} I_{1\sigma}^{qs}. \tag{22}$$

where a, as is shown by Redaelli and di Prisco,[27] is a dimensionless coefficient related to the interparticle friction coefficient μ_p, as it follows:

$$a = 0.75\mu_p + 1.23. \tag{23}$$

Function Φ, in Equation (21), is assumed to describe the dependency of dilatancy on the stress level as it follows:

$$\Phi = 3\sqrt{\frac{3}{2}} \frac{J_s^{qs}}{I_{1\sigma}^{qs}} - M_{cs}\left(\alpha_\sigma\right), \tag{24}$$

where $M_{cs}(\alpha_\sigma)$, the function describing the dependence on the Lode angle of the stress state obliquity at critical state, is given in Subsection 3.2.5.

3.2.4 | Hardening rules

With respect to the model of di Prisco et al.,[49] in this paper, the hardening variables $\boldsymbol{\chi}$ and r_c (Equation 15) evolution laws depend not only on plastic strains and current state of stress but also on Ψ:

$$\dot{\boldsymbol{\chi}} = \dot{k}\ [\hat{\boldsymbol{\chi}} - \boldsymbol{\chi}\,(\boldsymbol{\chi} : \hat{\boldsymbol{\chi}})] \tag{25}$$

$$\dot{k} = c_p\,(\Psi)\,\sqrt{\dot{\boldsymbol{\varepsilon}}^p : \dot{\boldsymbol{\varepsilon}}^p} \tag{26}$$

where

$$c_p\ (\Psi) = c_{pc}\ - c_{p\psi}\,\Psi, \tag{27}$$

being c_{pc} and $c_{p\psi}$ two nondimensional constitutive parameters.

This formulation is based on the assumption that $\dot{\boldsymbol{\chi}}$ obeys to a saturation rule, so that the higher the distance of $\boldsymbol{\chi}$ from the limit tensor $\hat{\boldsymbol{\chi}}$, the faster is the rotation.[49] $\dot{k}$ is a sort of activation scalar variable, function of $\dot{\boldsymbol{\varepsilon}}^p$ (Equation 26), and c_p, linearly variable with Ψ (Equation 27). $\hat{\boldsymbol{\chi}}$ is the limit tensor towards which $\boldsymbol{\chi}$ is assumed to evolve (Equation 25). According to di Prisco et al.,[49] $\hat{\boldsymbol{\chi}}$ is individuated by employing the mapping rule defined here below:

$$\hat{\boldsymbol{\chi}} = \cos\hat{\theta}\frac{\boldsymbol{I}}{\sqrt{3}} + \frac{\boldsymbol{d}}{\|\boldsymbol{d}\|}\sin\hat{\theta} \tag{28}$$

with

$$\boldsymbol{d} = \sqrt{3}\frac{\boldsymbol{s}^{qs*}}{r} - \left(\frac{\sqrt{3}}{3}\frac{\boldsymbol{s}^{qs*}}{r} : \boldsymbol{I}\right)\boldsymbol{I} \tag{29}$$

Differently from the model of di Prisco et al.,[49] the limit rotation angle $\hat{\theta}$ is assumed not only to depend on α_σ, but also on Ψ, that is:

$$\hat{\theta}\ (\Psi, \alpha_\sigma) = \frac{1}{2}\,\theta_{cc}\left[\left(1 + \frac{\theta_{ec}}{\theta_{cc}}\right) + \left(1 - \frac{\theta_{ec}}{\theta_{cc}}\right)\cos 3\alpha_\sigma\right] - \theta_\psi\,\Psi, \tag{30}$$

where θ_{cc}, θ_{ec} and θ_ψ are three non-dimensional constitutive parameters.

The evolution of r_c, tuned by a non dimensional constitutive parameter B_p, is defined as the sum of two contributions:

$$\dot{r}_c = r_c\left[\frac{\dot{\boldsymbol{\varepsilon}}^p : \boldsymbol{\chi} + \xi\,(\Psi, \alpha_\sigma)\,([\dot{\boldsymbol{\varepsilon}}^p - (\dot{\boldsymbol{\varepsilon}}^p : \boldsymbol{\chi})\boldsymbol{\chi}] : [\dot{\boldsymbol{\varepsilon}}^p - (\dot{\boldsymbol{\varepsilon}}^p : \boldsymbol{\chi})\boldsymbol{\chi}])^{\frac{1}{2}}}{B_p}\right], \tag{31}$$

one pseudo-volumetric and one pseudo-deviatoric (in fact, in case $\boldsymbol{\chi} = \boldsymbol{I}/\sqrt{3}$, the first contribution coincides with the plastic volumetric strain rate, while the second with the deviatoric one[51,52]).

In Equation (31), ξ is not constant, as it was in di Prisco et al.,[49] but is assumed to depend linearly on Ψ:

$$\xi\ (\Psi, \alpha_\sigma) = \hat{\xi}\ (\alpha_\sigma) - \xi_\psi\,\Psi, \tag{32}$$

being ξ_ψ a non-dimensional constitutive parameter, whereas the expression:

$$\hat{\xi}\ (\alpha_\sigma) = -\frac{\sqrt{3}}{2}\tan(\theta_{cc})\left[\left(1 + \frac{\tan(\theta_{ce})}{\tan(\theta_{cc})}\right) + \left(1 - \frac{\tan(\theta_{ce})}{\tan(\theta_{cc})}\right)\cos 3\alpha_\sigma\right], \tag{33}$$

is obtained by imposing $\dot{r}_c = 0$ at critical state.

TABLE 1 Values of micromechanical input data

ρ_p (kg/m^3)	d (m)	E_p (MPa)	μ_p (–)	ε_n (–)
2600	0.001	750	0.35	0.90

TABLE 2 Values of the constitutive parameters governing collisional response

e_m (–)	e_{cc} (–)	e_{ce} (–)
1.5	0.685	0.692

3.2.5 | Critical state locus

According to the model proposed, the critical state locus is a function of (i) state of stress, (ii) void ratio and (iii) five constitutive parameters (two micro, E_p, μ_p and three macro, e_{cc}, e_{ce}, γ). Its expression is obtained by nullifying the previously mentioned Ψ and Φ functions (Equations 22 and 24):

$$\Psi = e - e_c\left(\alpha_\sigma\right) + \frac{2}{3aE_p} I_{1\sigma}^{qs} = e - \frac{1}{2}\left[\left(e_{cc} + e_{ce}\right) + \left(e_{cc} - e_{ce}\right)\cos 3\alpha_\sigma\right] + \frac{2}{3aE_p} I_{1\sigma}^{qs} = 0, \tag{34}$$

$$\Phi = 3\sqrt{\frac{3}{2}}\frac{J_s^{qs}}{I_{1\sigma}^{qs}} - M_{cs}\ \left(\alpha_\sigma\right) = 0. \tag{35}$$

In the proposed model, $M_{cs}(\alpha_\sigma)$ is assumed to coincide with Matsuoka and Nakai[53] criterion, written in an explicit form by Lagioia and Panteghini[54]:

$$M_{cs} = 3\left[2\sqrt{\frac{\gamma-1}{\gamma-3}}\cos\left[\frac{1}{3}\arccos\left(\frac{\gamma\left(\gamma-3\right)^{1/2}}{\left(\gamma-1\right)^{3/2}}\sin 3\left(\alpha_\sigma - \frac{\pi}{6}\right)\right)\right]\right]^{-1}. \tag{36}$$

4 | CONSTITUTIVE PARAMETER CALIBRATION

To calibrate the constitutive model parameters, the authors employed the results of two DEM triaxial tests performed under constant confining pressure ($I_{1\sigma}$ =150 kPa) on an initially loose specimen (initial void ratio $e_0 = 0.727$): one compression ($\alpha_\sigma = 0°$, Figure 5) and one extension ($\alpha_\sigma = 60°$). In Appendix A, a detailed description of the DEM numerical model is reported.

As a comparison, in this paper the authors adopt numerical data referred to an ideal dry material characterised by identical frictional spheres.[1] Considering monodisperse materials seems reasonable since the aim of the work is to interpret and understand the fundamentals of granular material behaviour experiencing phase transitions. Moreover, as kinetic theories of granular gases have been validated until now for monodisperse media, considering a unitary coefficient of uniformity bears a discussion on advantages and liabilities of this approach when collisional contribution is dominant.

The response of the collisional contribution is governed by the geometry (grain diameter d) and physical/mechanical properties of the single particle (grain density ρ_p, grain Young modulus E_p, friction coefficient μ_p and coefficient of restitution ε_n): these are input data (Table 1) not to be calibrated and, for the monodisperse material considered in the paper, assumed to coincide with those employed to perform DEM numerical analyses (Appendix A).

Thirteen are the constitutive parameters related to the quasi-static contribution ($E, \nu, \beta, \gamma, \delta_1, \delta_2, \theta_{cc}, \theta_{ec}, \theta_\psi, c_{pc}, c_{p\psi}, B_p, \xi_\psi$). e_{cc} and e_{ce} define the dependence of the critical void ratio on Lode angle (Equation 12, Figure 3) and can be estimated by considering DEM results at critical state (compression and extension) (Table 2).

e_m, related to the collisional contribution (Appendix B), is taken from Berzi and Jenkins.[43]

Among the 13 constitutive parameters governing solely the quasi-static mechanical behaviour:

- E, ν describe the elastic material stiffness (Subsection 3.2.1).

[1] Numerical assemblies composed by monodisperse spheres may experience crystallization, but data that are considered in this paper are not affected by this phenomenon, since, as was discussed in Redaelli and di Prisco,[28] particles are not frictionless.

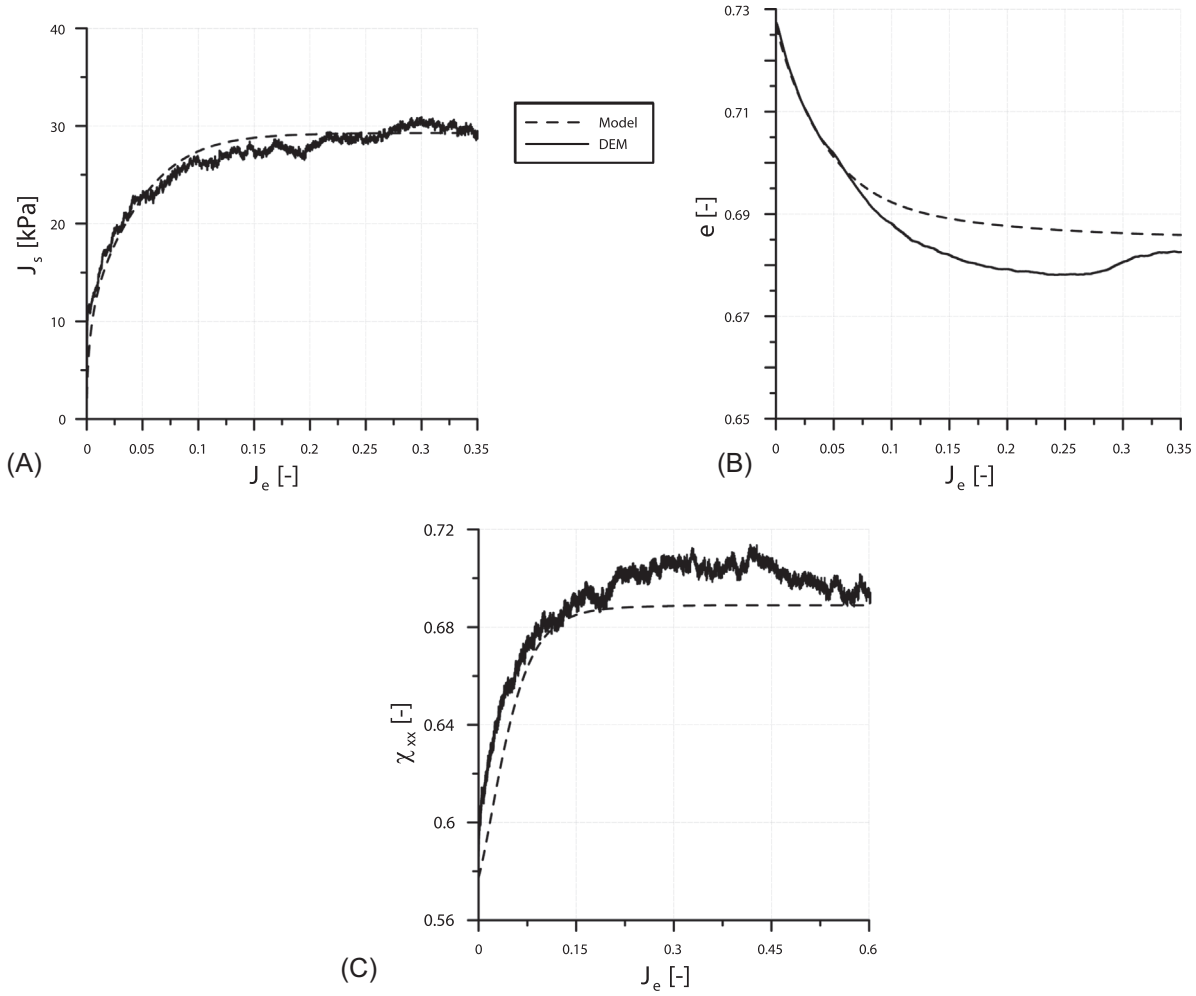

FIGURE 5 Comparison between discrete element method (DEM) results and model predictions in the (A) $J_s - J_e$ plane, (B) $e - J_e$ plane and (C) $\chi_{xx} - J_e$ plane

- β and γ define the shape of the yield locus (Subsection 3.2.2). The value of γ is directly connected to the size of the critical state locus (Subsection 3.2.5).
- δ_1 and δ_2 are related to the flow rule definition (Subsection 3.2.3).
- θ_{cc}, θ_{ec} are the limit values of back-stress rotation under compression and extension respectively, while θ_ψ defines its variation with Ψ, whereas c_{pc} and $c_{p\psi}$ govern the rotation velocity with strain rate (Subsection 3.2.4).
- B_p and ξ_ψ are parameters governing the isotropic hardening (Subsection 3.2.4).

Here below, the strategy employed to calibrate the 13 parameters listed here above:

1. E and ν have been calibrated by considering the very first part of the triaxial test in the $J_s - J_e$ plane (Figure 5A), where $J_s = [\frac{1}{3}[(\sigma_x - \sigma_y)^2 + (\sigma_x - \sigma_z)^2 + (\sigma_y - \sigma_z)^2]]^{1/2}$ and $J_e = [\frac{1}{3}[(\varepsilon_x - \varepsilon_y)^2 + (\varepsilon_x - \varepsilon_z)^2 + (\varepsilon_y - \varepsilon_z)^2]]^{1/2}$.
2. $\theta_{cc}, \theta_\psi, c_{pc}$ and $c_{p\psi}$ have been calibrated on the $\chi_{xx} - J_e$ plane (Figure 5C). For the DEM tests $\boldsymbol{\chi}$ is assumed to be equal to $\boldsymbol{\chi} = \frac{\hat{\boldsymbol{F}}}{|\hat{\boldsymbol{F}}|}$, where $\hat{\boldsymbol{F}}$ is the fabric tensor calculated from DEM data (Appendix A). In particular θ_{cc} is related to the final value of fabric orientation, c_{pc} to the initial slope of the curve, while θ_ψ and $c_{p\psi}$ govern the intermediate evolving condition.
3. γ, β, ξ_ψ have been calibrated focusing on the $J_s - J_e$ plane (Figure 5A). γ is calibrated to match the value at steady state, β the first part of the curve and ξ_ψ the transient condition.
4. B_p, δ_1 and δ_2, have been calibrated on the void ratio $e - J_e$ plane (Figure 5B).

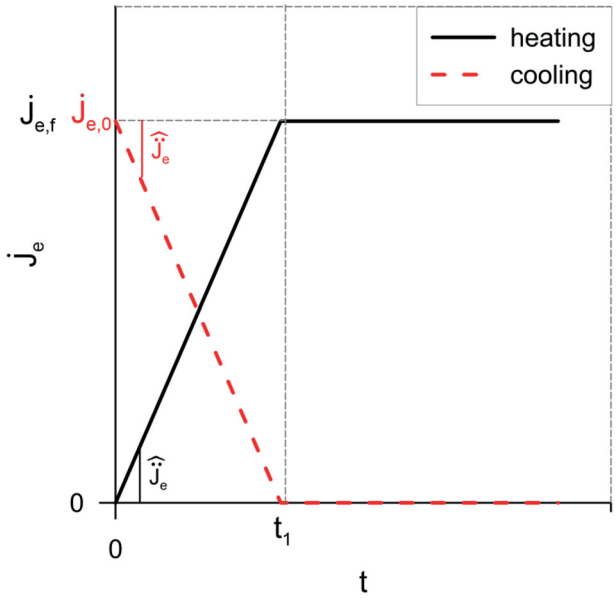

FIGURE 6 Time evolution of the deviatoric strain rate in case of heating tests (solid line) and cooling tests (dashed line)

5. Finally, θ_{ce} has been calibrated by considering steady state condition of quasi-static constant pressure triaxial tests under extension, focusing on the final point of the curve in the $\chi_{xx} - J_e$ plane.

The procedure employed to generate DEM specimen (Appendix A) determines a strong homogeneity in the specimen microstructure. In case of quasi-static isotropic consolidation tests, commonly employed in case of real granular materials to calibrate B_p, the lack of heterogeneity of DEM numerical specimens seems not to allow the evolution of the microstructure under isotropic conditions and their use for calibration purposes. In fact, loading-unloading DEM curves practically superimpose.[13,55] For the same reason, in case of initially dense materials (Subsection 5.1.2), due to the very large number of interparticle contacts, DEM curves relative to constant pressure triaxial tests, are characterised by a very large initial stiffness, not easily reproducible by the constitutive model.

5 | MODEL VALIDATION

In this section, to test the model capability of simulating the dependence of the material mechanical behavior on the (i) imposed strain rate, (ii) stress path and (iii) initial void ratio, model predictions are compared with DEM numerical results (true triaxial monotonic tests). In Appendix A, a detailed description of the DEM numerical tests is reported.

To simulate both inception and arrest of granular flows, two types of tests are considered: (i) heating and (ii) cooling, respectively (Figure 6).

In case of heating, the material is initially at rest, isotropically consolidated at confining pressure $I_{1\sigma}$ and initial void ratio e_0.

Then, the deviatoric strain rate is imposed to vary with time according to the following function (solid line in Figure 6):

$$\dot{J}_e\ (t) = \begin{cases} \frac{j_{e,f}}{t_1} \cdot t & \text{if } t < t_1 \\ \dot{J}_{ef} & \text{if } t \geq t_1 \end{cases}, \tag{37}$$

where $t_1 = \frac{|j_{e,f}|}{\dot{\hat{J}}_e}$ and $\dot{\hat{J}}_e[\mathrm{s}^{-2}]$ are the rate of change in the deviatoric strain rate (strain acceleration).

During cooling tests, the material is initially flowing under steady triaxial condition, coinciding with the final state reached at the end of a heating test.

TABLE 3 Values of the constitutive parameters governing quasi-static response only

Elastic stiffness		Yield function		Flow rule		Kinematic hardening					Isotropic hardening	
E (MPa)	ν (–)	β (–)	γ (–)	δ_1 (–)	δ_2 (–)	θ_{cc} (–)	θ_{ce} (–)	θ_{ψ} (–)	c_{pc} (–)	$c_{p\psi}$ (–)	B_p (–)	ξ_{ψ} (–)
500	0.3	0.5	3.185	4.7	0.8	0.145	0.129	0.5	35	640	0.001	3.4

TABLE 4 List of model heating tests

Test name	e_0 (–)	α_σ (°)	$I_{1\sigma}$ (kPa)	$\dot{J}_{e,f}$ (s^{-1})	$\hat{\dot{J}}_e$ (s^{-2})
M_H_0-10_1	0.727	0	150	10	1e6
M_H_0-100_2	0.727	0	150	100	1e6
M_H_0-10_3	0.657	0	150	10	1e6
M_H_0-10_4	0.727	30	150	10	1e6
M_H_0-10_5	0.727	60	150	10	1e6
M_H_0-10_10	0.727	0	15	10	1e6
M_H_0_10_1_CV	0.727	0	150	10	1e6
M_H_0_10_2_CV	0.727	0	150	100	1e6

Then, the strain rate is linearly decreased to zero (dashed line in Figure 6):

$$\dot{J}_e\ (t) = \begin{cases} \dot{J}_{e,0} - \frac{\dot{J}_{e,0}}{t_1} \cdot t & \text{if } t < t_1 \\ 0 & \text{if } t \geq t_1 \end{cases}, \tag{38}$$

where $t_1 = \frac{\dot{J}_{e,0}}{\hat{\dot{J}}_e}$ and $\hat{\dot{J}}_e[s^{-2}]$ are the rate of change in the deviatoric strain rate (strain deceleration).

To obtain model predictions, Equations (2, 3, 4, 25, 31) are numerically integrated in time, by imposing a sufficiently small time-step, to guarantee numerical stability and by imposing: (i) the total mean pressure $I_{1\sigma}$ and Lode angle α_σ to be constant, (ii) the deviatoric strain rate $\dot{J}_e$ to evolve according to Equations (37) or (38). The nonzero initial conditions for heating and cooling tests are discussed in Subsections 5.1 and 5.2, respectively.

5.1 | Heating tests

Heating tests, whose results are discussed in the following, are listed in Table 4 and are identified by the acronym 'M_H_0_$\dot{J}_{e,f}$_i', where i is an identification number. In Table 4, the nonzero initial conditions, the final strain rate, the Lode angle and the acceleration rate of the eight tests, whose results are discussed here below, are reported.

5.1.1 | Influence of α_σ

To investigate the influence of Lode angle, three 'constant pressure' tests ($I_{1\sigma} = 150$ kPa with $\dot{J}_{e,f} = 10\ s^{-1}$) characterised by $\alpha_\sigma = 0°, 30°, 60°$, respectively, are considered. In all the three cases (M_H_0-10_1, M_H_0-10_4, M_H_0-10_5), the material is initially loose ($e_0 = 0.727$).

As is evident in Figure 7, the agreement between model predictions (dashed lines) and DEM data (solid lines), in particular in the $J_s - J_e$ plane (Figure 7A), is quite satisfactory. Initially, the deviatoric stress increases very rapidly and the material response is independent of α_σ. Subsequently, the dependence on α_σ becomes clearer: larger J_s values correspond to smaller α_σ values. In Figure 7B, where the volumetric response is shown, the dependence on α_σ is correctly captured, although at large strains ($J_e > 0.1$) model simulations seem to overestimate void ratio. According to the authors, this is mainly due to the DEM data oscillating trend. In fact, at steady state DEM and model predictions practically superimpose. In Figure 7C strain paths for $\alpha_\sigma = 30°$ (imposed load direction) are plotted in the $J_s - \alpha_\varepsilon$ deviatoric plane. As is evident, strain paths deviate from the imposed stress path and the non-coaxialitly seems to be correctly simulated by the theoretical model, in particular for large strains.

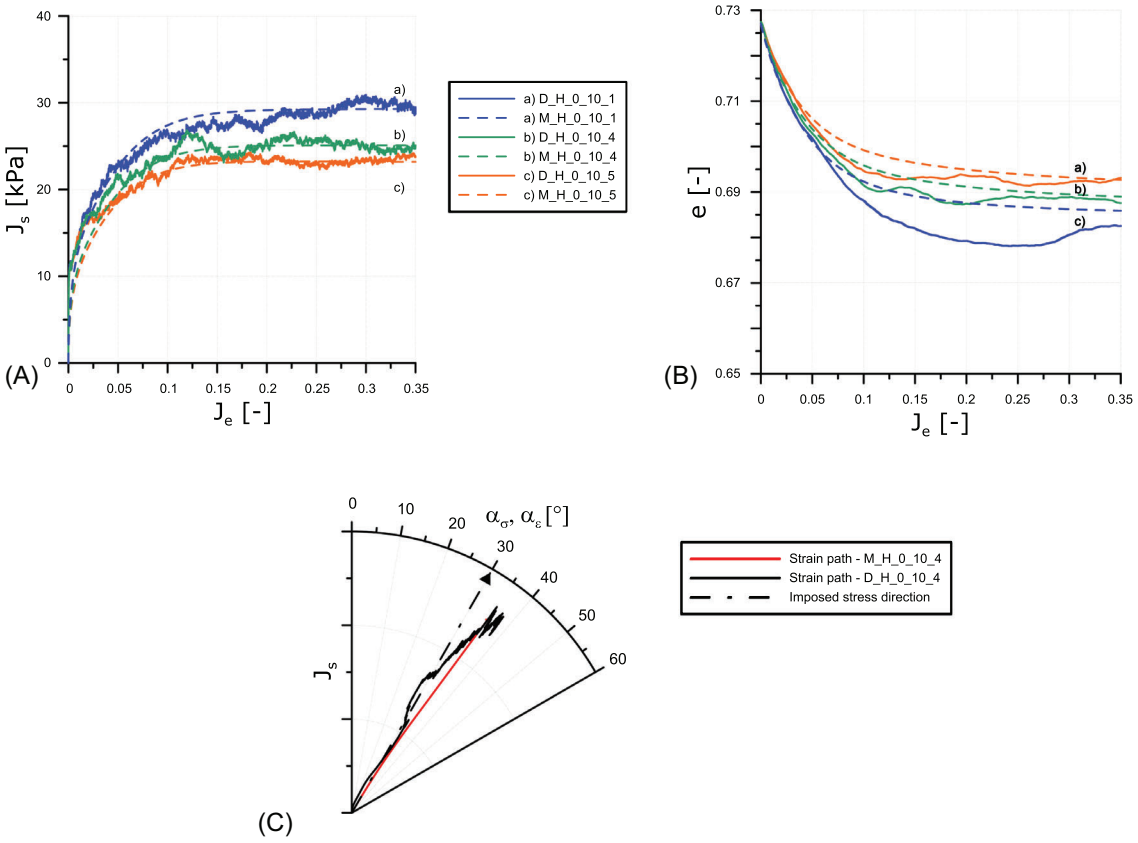

FIGURE 7 Influence of Lode angle. Comparison between discrete element method (DEM) results and theoretical model predictions in (A) $J_s - J_e$, (B) $e - J_e$ and (C) $J_s - \alpha_\sigma$ planes

5.1.2 | Influence of initial void ratio

Two constant pressure compression tests ($I_{1\sigma} = 150$ kPa, $\alpha_\sigma = 0°$), characterised by $\dot{J}_{e,f} = 10\ s^{-1}$, are here considered. Test M_H_0-10_1 corresponds to $e_0 = 0.727$, whereas test M_H_0-10_3 to $e_0 = 0.657$.

The theoretical model is capable of capturing, both qualitatively and quantitatively, the dependence of the evolving response on initial void ratio. As is evident in Figure 8A, the model predicts quite well DEM simulations. The dense specimen response presents a faint peak in DEM data, predicted also by the model, but the DEM curve is characterised by an initial stiffer behaviour. As was anticipated in Section 4, this discrepancy is likely to be due to the particular initial homogeneity of monodisperse DEM specimen, causing, in case of dense conditions, an increase in contacts along vertical direction even without initial microstructure rearrangement (Figure 8C).

The volumetric behaviour ($e - J_e$ plane) is illustrated in Figure 8B: a compacting response is observed for both DEM and model predictions in case of loose initial conditions (again DEM data are characterised by oscillations at large strains), in contrast, dense specimens, for both DEM and model predictions, dilate. According to the authors, the DEM specimen, for the same reason mentioned above (Section 4), cannot initially compact. At steady state, as was expected, the void ratio is independent of the initial value of e_0. Finally, in Figure 8C, the evolution of fabric orientation (in terms of the first component of tensor χ) predicted by the model is compared with the corresponding DEM data: the agreement is very satisfactory.

5.1.3 | Influence of strain rate

Two 'constant pressure' tests ($I_{1\sigma} = 150$ kPa, $\alpha_\sigma = 0°$) on loose specimens ($e_0 = 0.727$), characterised by different final strain rates and coincident initial strain accelerations (Figure 6) are simulated: in one case $\dot{J}_{e,f} = 10\ s^{-1}$ (M_H_0-10_1), while in the other $\dot{J}_{e,f} = 100\ s^{-1}$ (M_H_0-100_2).

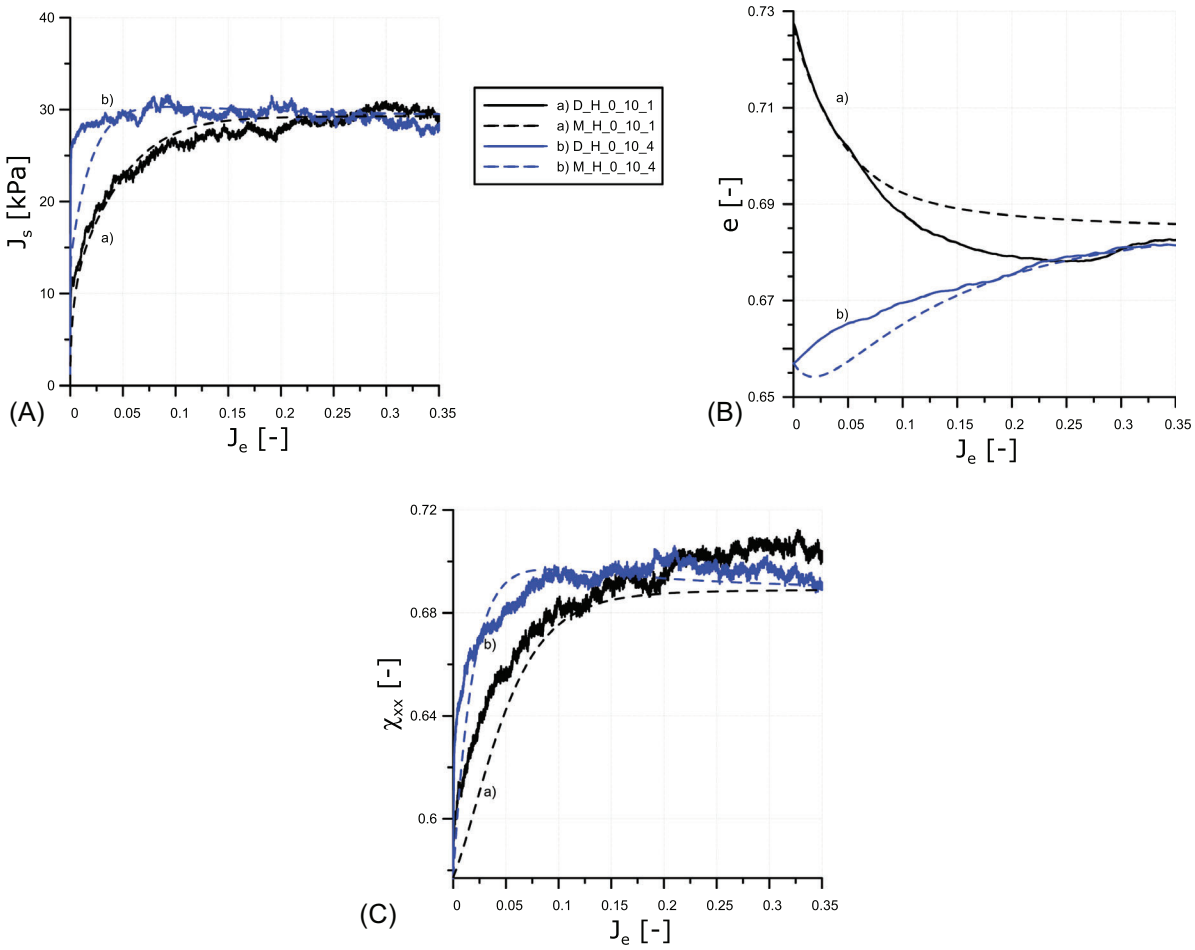

FIGURE 8 Influence of initial void ratio. Comparison between discrete element method (DEM) results and theoretical model predictions: (A) $J_s - J_e$, (B) $e - J_e$ and (C) $\chi_{xx} - J_e$ planes

In Figure 9, model simulations (dashed lines) and DEM results (solid lines) are compared. The model is capable of capturing the dependence at steady state of J_s and e values on the imposed strain rate (larger values of $\dot{J}_e$ correspond to larger J_s and e values). As was expected, the initial trend of DEM curve is not correctly reproduced by the model, in which micro-inertial terms governing the evolution of force chains with time are not accounted for.[56–59] For the same reason in the J_e–e plane (Figure 9B), the more pronounced dependence of the volumetric response on the strain rate imposed, exhibited by the DEM specimen, is not fully simulated by the model, since again, according to the authors, this does not take into account micro-inertia.

The model capability of predicting DEM data in terms of fabric orientation is illustrated in Figure 10, where the evolution of the first component of tensor χ is plotted and compared with the corresponding value of fabric predicted by DEM. For very large values of strain rate, the anisotropy of the fabric tensor increases with the shear rate imposed. This aspect is not reproduced by the model since no microstructure anisotropy is taken into account by kinetic theories.

5.1.4 | Model discussion

In this paragraph, with reference to heating tests, the authors want to discuss phase transitions starting from the analysis of the constitutive model predictions, by focussing on the role of quasi-static and collisional contributions.

Phase transition, as is predicted by $\mu - I$ rheology,[26] is favoured by an increase in I, that is by an increase in deviatoric strain rate or a reduction in confining pressure.

As far as the role of $\dot{J}_{e,f}$ is concerned, apparently, at steady state, the two curves of Figure 9A are very similar. In contrast, as already mentioned in Section 2 (Figures 1 and 2), the authors want to show that the mechanical behaviour of the material

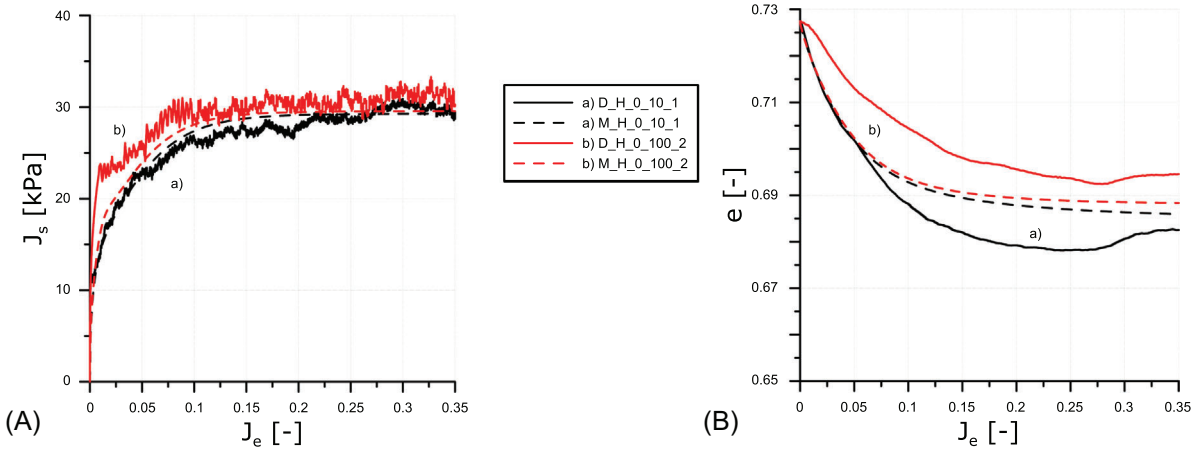

FIGURE 9 Influence of strain rate. Comparison between discrete element method (DEM) results and theoretical model predictions in: (A) $J_s - J_e$ and (B) $e - J_e$ planes

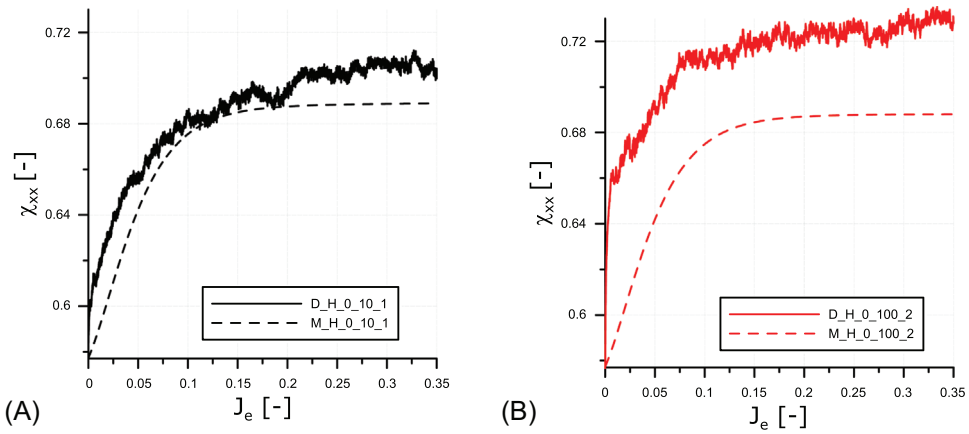

FIGURE 10 Comparison between discrete element method (DEM) results and theoretical model predictions in $\chi_{xx} - J_e$ plane: (A) test M_H_0-10_1, (B) test M_H_0-100_2

is totally different and governed by two distinct dissipative microstructural mechanisms. In Figure 11, total stresses (solid line), quasi-static (dashed line) and collisional (dot-dashed line) stresses are compared. The discussion is limited to model predictions since, as is discussed in Redaelli and di Prisco,[28] in DEM, collisional and quasi static (permanent) contributions cannot be isolated to each other.

In case $\dot{J}_{e,f} = 10\ s^{-1}$ (Figure 11A), the collisional stress slightly increases during the test, but the quasi-static contribution prevails and the steady state is reached only for very large values of the deviatoric strain ($J_e > 0.8$). In case $\dot{J}_{e,f} = 100\ s^{-1}$ (Figure 11B), initially, the quasi-static contribution prevails. For $J_e > 0.05$, the quasi-static contribution progressively decreases whereas the collisional one increases. When large values of deviatoric strain are reached, the quasi-static contribution is almost negligible and the total stress coincides with the collisional one. The 'dry' liquefaction of the specimen sheared at $\dot{J}_{e,f} = 100\ s^{-1}$ is evident in Figure 11C, where the quasi-static (line b1) and collisional (line b2) stress paths are plotted. In contrast, in case $\dot{J}_{e,f} = 10\ s^{-1}$, the quasi-static pressure (line a1) remains dominant, almost coinciding with the total one.

The corresponding evolution of r_c is plotted in Figure 11D: in case $\dot{J}_{e,f} = 100\ s^{-1}$ (line b), r_c nullifies, meaning that the effect of the previous strain history 'survives' in terms of microstructure orientation (Figure 10), but not in terms of yield locus size, suggesting a total disruption of the force chains network. In contrast, in case of test M_H_0-10_1 ($\dot{J}_{e,f} = 10\ s^{-1}$), the reduction in r_c is marginal (line a), since the quasi-static contribution prevails on the fluctuating one.

To discuss phase transition from an energetic point of view, in Figure 12, the evolution of elastic ($E_{qs,el} = \frac{1}{2}\boldsymbol{D}^{el} : \boldsymbol{\varepsilon}^{el} : \boldsymbol{\varepsilon}^{el}, E_{f,el}$) and kinetic energies ($E_{f,k}$), normalised by the total energy stored by the system ($E_{st} = E_{f,k} + E_{f,el} + E_{qs,el}$) is plotted for both DEM (D_H_0_100_2) and model (M_H_0_100_2). Both DEM and model predict:

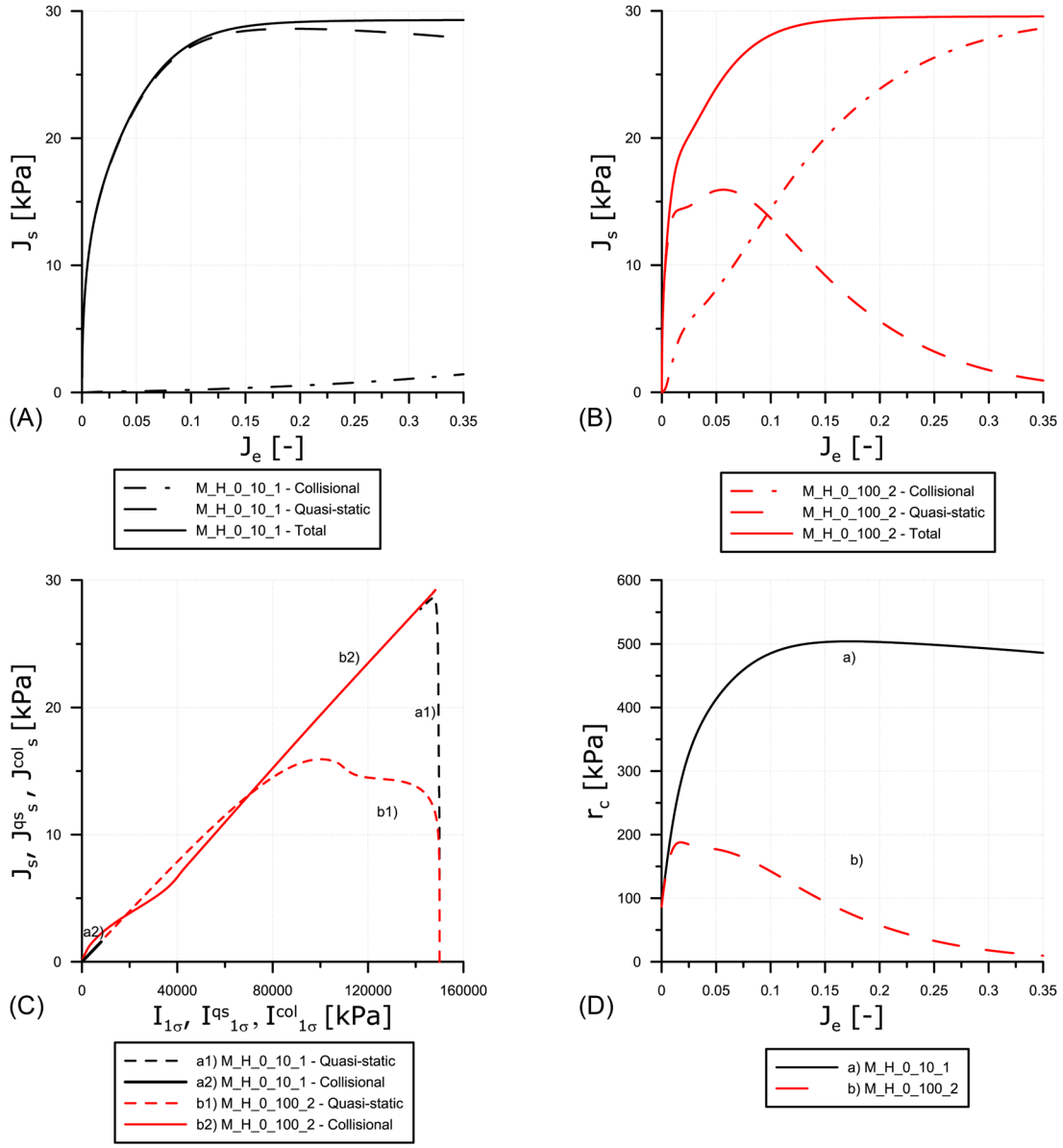

FIGURE 11 Influence of strain rate (M_H_0-10_1 and M_H_0-100_2). Model predictions in (A) $J_s - J_e$ plane (test M_H_0-10_1), (B) $J_s - J_e$ plane (test M_H_0-100_2), (C) $I^{qs}_{1\sigma}$–J^{qs}_s plane and (D) $r_c - J_e$ plane

(i) the energy initially being fully elastically stored in force chains ($E_{qs,el}/\ E_{stor} = 1$ and $E_f/\ E_{stor} = 0$), since the specimen is initially static;
(ii) during the simulation, the elastic energy ($E_{el} = E_{qs,el}\ + E_{f,el}$) markedly reducing in favour of kinetic fluctuating energy, due to the high deviatoric strain rate imposed.
(iii) for $J_e = 0.007$, the fluctuating energy becoming the main stored energy contribution, exceeding the elastic one, as the material undergoes phase transition;
(iv) an elastic energy not collapsing to 0, since the system is able to store elastic energy during collisions owing to particle deformability.

By comparing Figure 11B–D and Figure 12, one can notice that, despite the phase transition occurrence is testified from an energetic point of view since the very beginning of the test, in terms of stress the phase transition occurrence could be postponed around $J_e = 0.08$. This poses the question on the actual definition of phase transition: due to the different nature of dissipation mechanism, the collisional contribution is able to store a large amount of energy without exhibiting large resistance, while on the contrary, the force chain system is able to sustain a large load, without large deformation

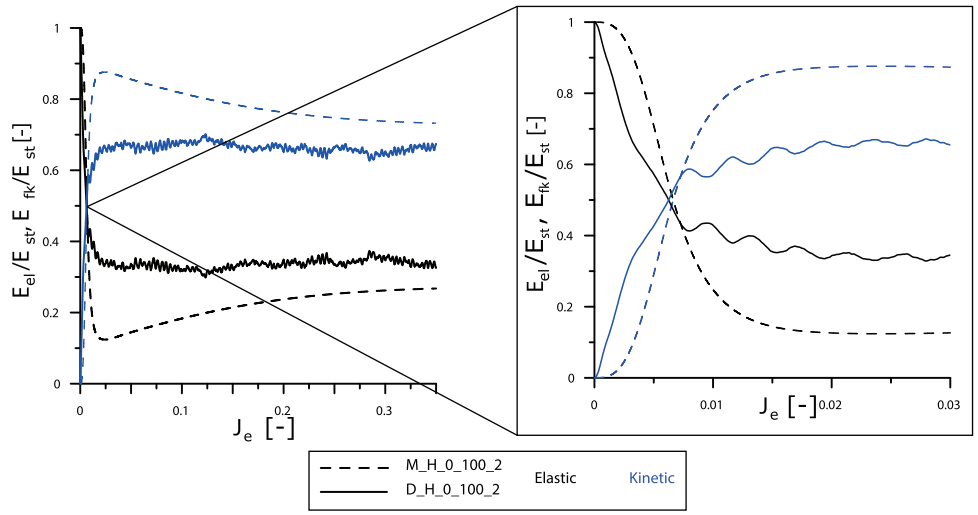

FIGURE 12 Stored energy contributions (tests M_H_0-100_2 and D_H_0-100_2): discrete element method (DEM) data and model predictions

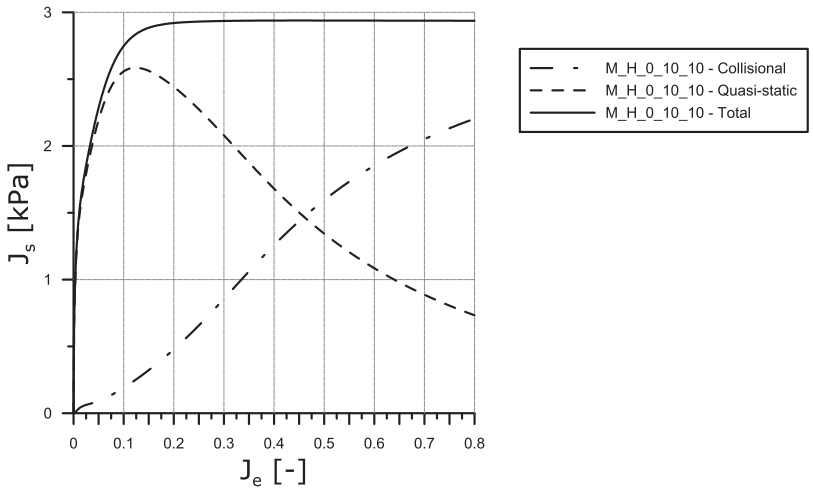

FIGURE 13 Model predictions in $J_s - J_e$ plane (test M_H_0-10_10): collisional, quasi-static and total contribution

and stored energy. This 'energetic' phase transition seems to slightly anticipate the one that can be detected by looking at the stress contribution.

To demonstrate the model capability of capturing the role of pressure in the phase transition process, in Figure 13, quasi-static, collisional and total stress contributions are plotted for test M_H_0_10_10, characterised by $\dot{J}_{e,f} = 10\ s^{-1}$ and $I_{1\sigma} = 15$ kPa. As is evident, although the $\dot{J}_{e,f}$ value imposed is coincident with that of M_H_0_10_1 (Figure 11A), the response resembles that of test M_H_0_100_2 (Figure 11B).

As is well known in geotechnical literature,[60–62] phase transition takes place in loose granular media when the specimen is sheared under constant volume conditions (that is undrained conditions if the material is saturated). Static liquefaction is the term used to describe the phenomenon associated with the nullification of effective pressure. To testify the model capability of reproducing also such a phenomenon, in Figure 14, the model numerical predictions under constant volume conditions (M_H_0-10_1_CV and M_H_0-100_2_CV) are illustrated. The model predictions put in evidence that: (i) the loss of controllability[63] (that is the peak in the J_s–$I_{1\sigma}$ plane, point H) takes place when the material is still behaving like a solid and the hardening variable r_c is still increasing,[28] (ii) phase transition is testified even by the abrupt reduction of r_c, that is when the yield function tends to degenerate into a point.

In Figure 14, numerical predictions refer to two different stain rates. Until phase transition does not occur, the numerical simulations perfectly coincide, since strain rate sensitivity does not play any role, as the quasi-static contribution prevails. In contrast, when phase transition takes place, the collisional contribution governs the mechanical behaviour of the material and the mechanical response of the two tests are totally different.

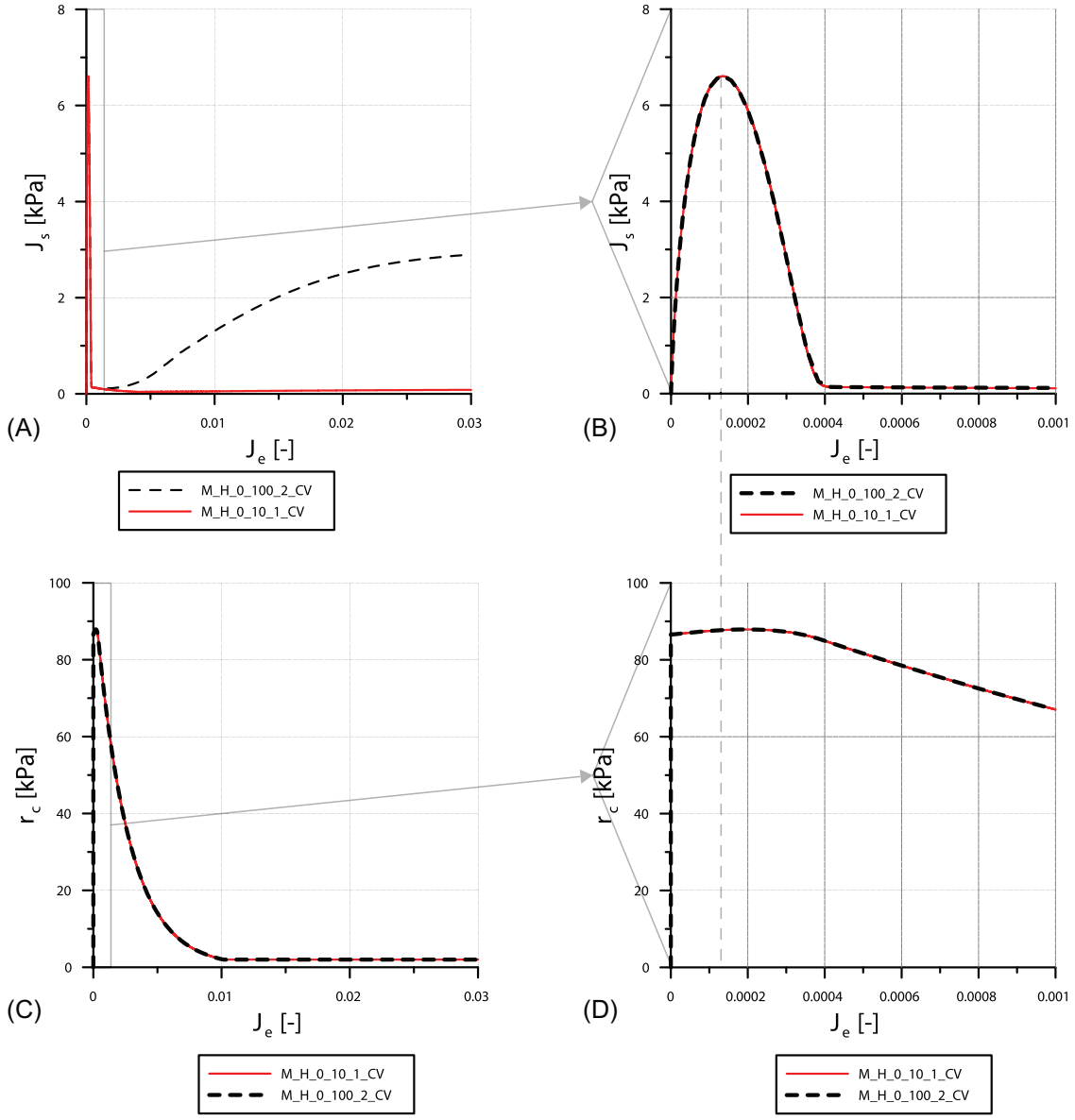

FIGURE 14 Influence of strain rate (M_H_0-10_1_Cv and M_H_0-100_2_Cv). Model predictions in (A) $J_s - J_e$ plane, (B) $J_s - J_e$ plane (magnified), (C) $I_{1\sigma} - J_s$ plane and (D) $r_c - J_e$ plane

5.2 | Cooling tests

In this section, the model is tested in case the granular specimen, starting from a steady shearing condition, is arrested (freezed to $\dot{J}_{e,f} = 0$).

Cooling tests are identified by the acronym 'M_C _$\dot{J}_{e,h}$_0_i', where i is an identification number.

In Table 5, the initial deviatoric strain rate and the deceleration rate of the four tests, whose results are discussed here below, are reported. The initial condition of each test coincides with the steady one of the corresponding heating test, reported in Table 5, for the sake of clarity.

Cooling tests M_C_100_0_7 and M_C_100_0_8 are characterised by the same initial steady condition with $\dot{J}_{e,h} = 100$ s^{-1}, but they differ for the deceleration imposed: the former one decelerates more rapidly. In Figure 15, DEM results are compared with model predictions in both $J_s - J_e$ and $e - J_e$ planes. The cooling tests seem to experience a sort of reconsolidation, tuned by the energy fluctuation balance (Equation 4), governing the granular temperature evolution with time. In the $J_s - J_e$ plane (Figure 15A, B), the model is shown to be capable of predicting DEM results. Most of the reduction in stress takes place at the end of cooling: the agitation stored energy (collisional) seems to require additional

TABLE 5 List of cooling tests performed

Test name	Test for initial conditions	$\dot{J}_{e,h}$ (s^{-1})	($\hat{\dot{J}}_e s^{-2}$)
M_C_10-0_6	M_H_0_10_1	10	1e6
M_C_100-0_7	M_H_0_100_2	100	1e6
M_C_100-0_8	M_H_0_100_2	100	1e5
M_C_100-0_9	M_H_0_100_2	100	1e4

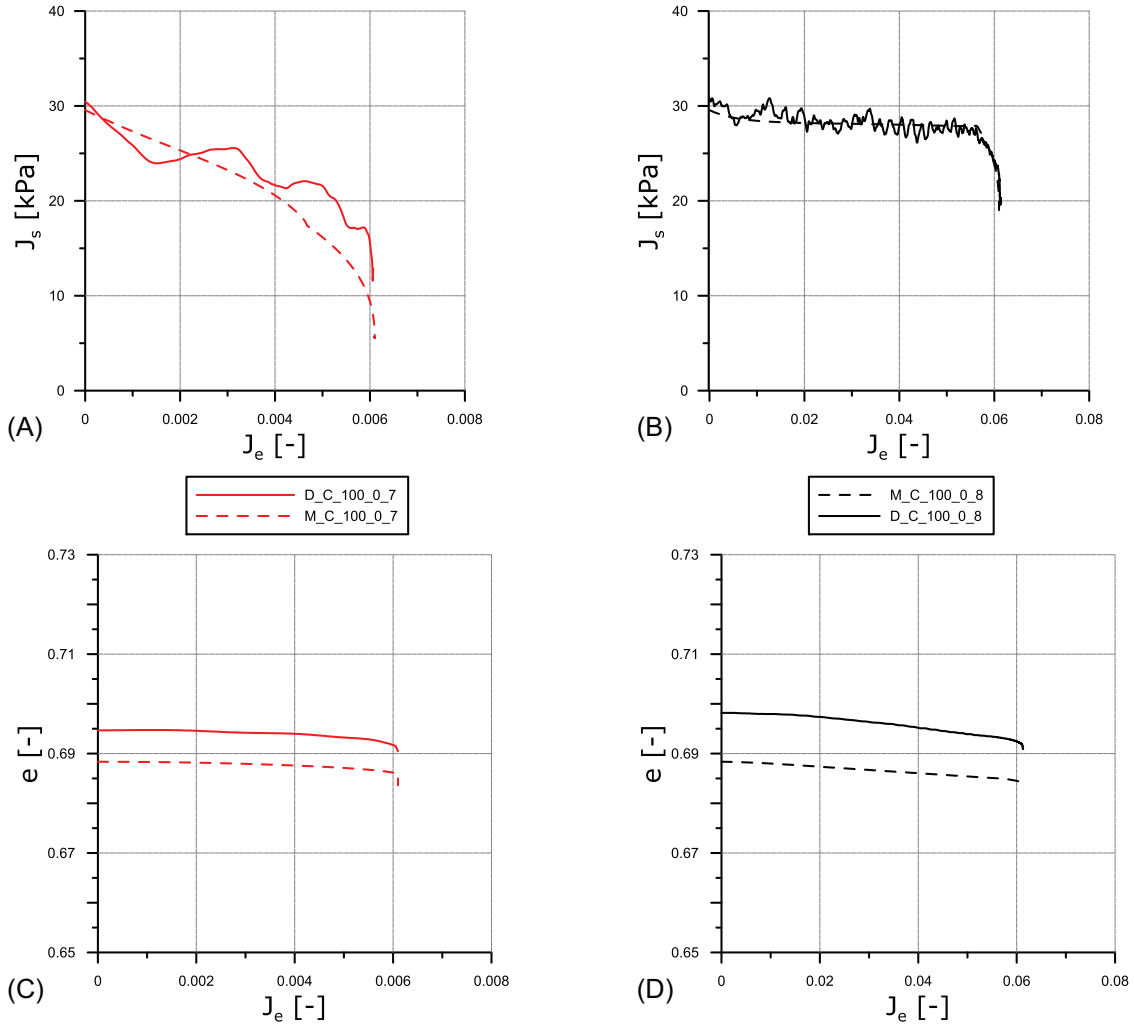

FIGURE 15 Comparison between discrete element method (DEM) results and theoretical model predictions in: (A) $J_s - J_e$ plane (D_C_100_0_7 and M_C_100_0_7), (B) $J_s - J_e$ plane (D_C_100_0_8 and M_C_100_0_8), (C) $e - J_e$ plane (D_C_100_0_7 and M_C_100_0_7), (D) $e - J_e$ plane (D_C_100_0_8 and M_C_100_0_8)

time to dissipate. The volume (Figure 15C, D) does not vary remarkably during the process, although a compaction is slightly more evident in test M_*C*_100-0_7.

As was already mentioned in Subsection 5.1.3, kinetic theories do not consider the material anisotropy, that is in the collisional regime the model back stress tensor is 'freezed'. This justifies the evolution of χ_{xx} in Figure 16A, B, that does not mimic the DEM results, showing a progressive reduction during the arrest. Nevertheless, at rest the agreement is satisfactory, as was expected since the collisional contribution nullifies.

The granular material, which has 'dry-liquefied' in the heating test M_H_0_100_2 (path A–B of Figure 17A), 'reconsolidates' according to different stress paths (B–C, B–D, B–E of Figure 17A) during the arrest process. Since collisional

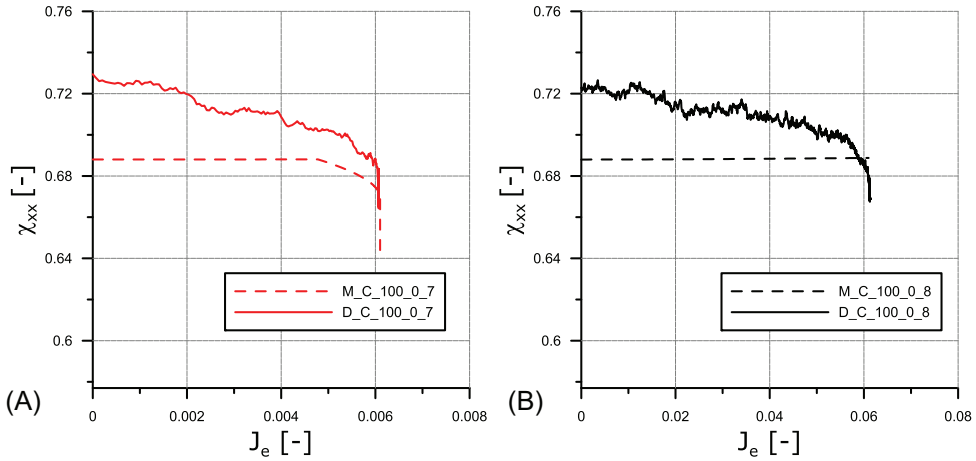

FIGURE 16 Comparison between discrete element method (DEM) results and theoretical model predictions in $\chi_{xx} - J_e$ plane: (A); $\dot{J}_{e,f} = 10^6$ s^{-2} (D_C_100_0_7 and M_C_100_0_7), (B) $\dot{J}_{e,f} = 10^6$ s^{-2} (D_C_100_0_8 and M_C_100_0_8)

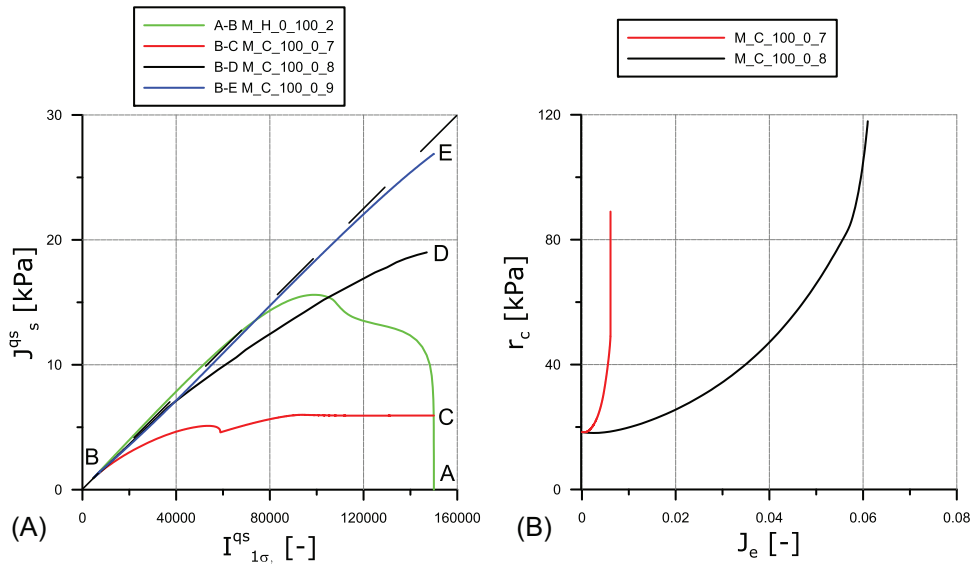

FIGURE 17 Influence of arrest time: theoretical model predictions on: (A) $J_s^{qs} - I_{1\sigma}^{qs}$ and (B) $r_c - J_e$ planes

contribution is initially not negligible, they do not all belonging to the critical state line (dashed line in Figure 17A) and the final obliquity is indeed a function of the arrest time.

In Figure 17B, the 'reconsolidation' process is described by focusing on the evolution of r_c. Larger values of decelerations cause a reduction in the accumulation of irreversible strains: this justifies the dependence of the final value of r_c on the imposed value of deceleration.

The model also seems to be capable of satisfactory reproducing DEM results even in case the initial strain rate value is smaller (M_C_10_0_6): in this case, during the test, J_s reduces (Figure 18A), whereas void ratio remains constant (Figure 18B).

5.3 | Model predictions: Influence of both initial strain rate and arrest time on the state of stress at rest

According to DEM data and in agreement with model predictions, the final state of stress (at rest) is a function of the previous strain rate history ($\dot{J}_{e,h}$). This dependency is illustrated in Figure 19 in terms of $\eta/M_{cs}(\alpha_\sigma)$ versus the arrest time

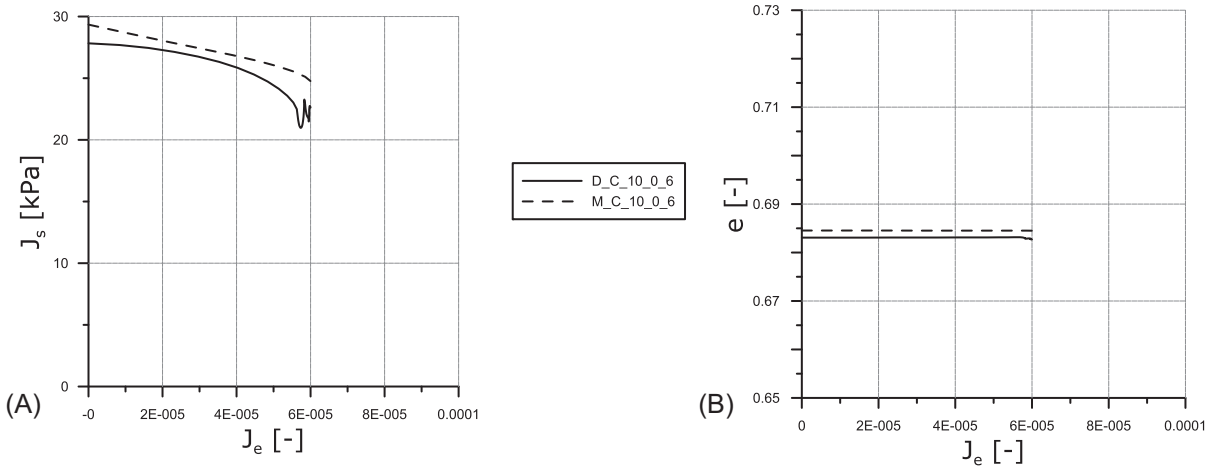

FIGURE 18 Comparison between discrete element method (DEM) results and theoretical model predictions (test M_C_10_0_6) in: (A) $J_s - J_e$ and (B) $e - J_e$ planes

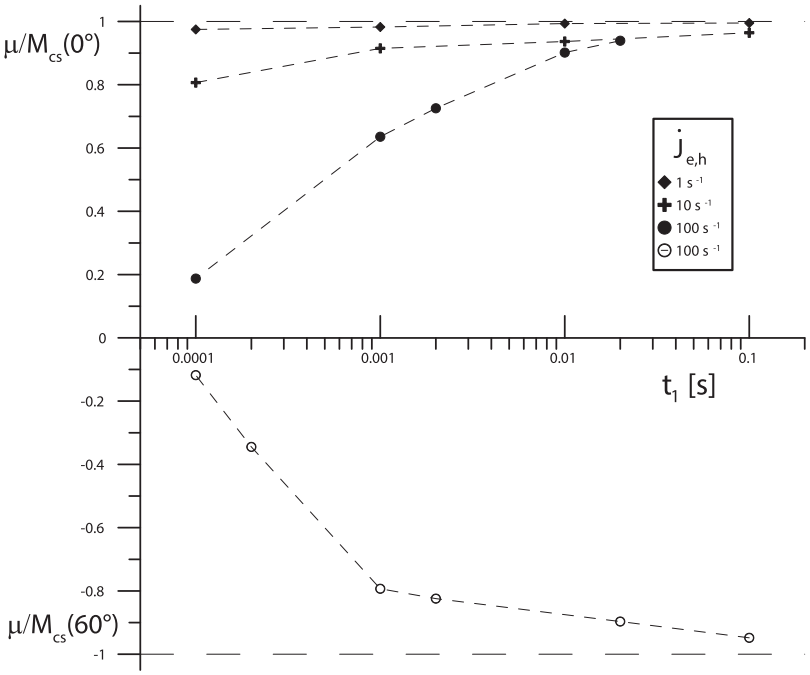

FIGURE 19 Model predictions: normalised stress level versus arrest time for both compression ($\eta/M_{cs}(0°)$) and extension ($\mu/M_{cs}(60°)$) loading paths

t_1 (Equation 38), where $\mu = 3\sqrt{\frac{3}{2}}\frac{J_s}{I_{1\sigma}}$ and the critical state obliquity M_{cs} is given by Equation (36). Each curve in Figure 19 corresponds to a different value of $\dot{J}_{e,h}$. In case the material is initially flowing under large strain rates, rapid arrest times leads to small values of obliquity at rest, that is to an almost isotropic state of stress. This effect tends to disappear when the initial strain rate $\dot{J}_{e,h}$ reduces. This confirms the dependence of the state of stress acting against obstacles under residual conditions on the velocity of the flowing mass, already numerically shown in Redaelli et al.,[64] where impacts of flowing masses on rigid obstacles were simulated by using a DEM code.

6 | CONCLUDING REMARKS

In this paper, the authors introduce a constitutive model capable of simulating the mechanical behaviour of ideal granular materials under quasi-static and dynamic evolving conditions. In particular, the model has been shown to be suitable for simulating the phase transition observed when the material is rapidly perturbated. The mathematical model is based on

both kinetic theories of granular gases and elastic-plasticity. The reinterpretation of the critical state as a steady condition ideally reached for vanishing values of inertial numbers has been considered to be fundamental for unifying the two theoretical worlds: one developed in the last thirty years within the hydraulics/physicists community, focused on steady agitated regimes and the other one, popular in the solid/geo mechanics community, interpreting the mechanical behaviour of granular materials under quasi-static evolving conditions. The model is based on the assumption that total stresses are obtained, according to a parallel scheme, by adding quasi-static and collisional contributions. With respect to the previous constitutive models, already conceived by the authors, all defined under simple shear conditions, in this new 3D version, three additional ingredients have been introduced: (i) the dependence of steady state on Lode angle, (ii) the mixed isotropic-anisotropic elastoplastic strain hardening and (iii) a closed-shape yield function. According to the authors, fundamental is the role of the isotropic hardening defining the size of the yield function when a phase transition has to be modelled. In fact, when phase transition takes place, the yield locus has to shrink and elastic locus has to nullify, since the material under fluidised conditions cannot store elastic energy by means of the development of a network of permanent force chains. In the model this result is obtained by modifying standard hardening rules according to critical state theories. Original is also the calibration/validation strategy of the model on DEM numerical results, according to which even the hardening rule of the fabric tensor is derived from the information relative to the description of the evolution of the microstructure.

The model is validated on both heating and cooling constant pressure true triaxial monotonic tests, on both loose and dense specimens under different imposed deviatoric strain rates. The comparison between DEM data and model simulations is quite satisfactory; this implies that the approach proposed is promising even for the simulation of the mechanical behaviour of natural granular materials, characterised for instance by not spherical shaped particles and a graded grain size. The comparison between model predictions and DEM data has also allowed to put in evidence some limitations of the model, very instructive for further developments.

Owing to the parallel scheme and the reinterpretation of the critical state in the light of kinetic theories of granular gases, the model seems to be suitable for describing from solid to fluid and vice versa phase transition phenomena, ruled by the evolution of void ratio and granular temperature.

As was previously mentioned, the solid-to-fluid transition is simulated by the model by means of the nullification of the isotropic-hardening variable, partially deleting the material memory, but without any change in the directional characteristic testified by the back-stress evolution. This constitutive hypothesis seems to be correct since DEM numerical results clearly show that, when phase transition takes place, the second invariant of the fabric tensor deviator does not nullify, but, in contrast, increases for very large values of strain rate. This theoretical observation put in evidence a limitation of kinetic theories that do not account for microstructure anisotropy, as they consider as state variables only void ratio and granular temperature.

NOMENCLATURES

$\boldsymbol{\sigma}$	total stress tensor
$\boldsymbol{\sigma}^{qs}$	quasi static stress tensor
$\boldsymbol{\sigma}^{col}$	collisional stress tensor
$\boldsymbol{\varepsilon}$	total strain tensor
$\boldsymbol{\varepsilon}^{el}$	elastic strain tensor
$\boldsymbol{\varepsilon}^{pl}$	plastic strain tensor
$\boldsymbol{D}^{el}$	quasi static elastic 4th order tensor
$\boldsymbol{D}^{qs}$	quasi static elasto-plastic 4th order tensor
$\boldsymbol{D}^{vep}$	visco-elasto-plastic 4th order tensor
$\boldsymbol{H}^{col}$	viscous collisional 4th order tensor
$\boldsymbol{h}^{col}$	bulk collisional second order tensors
e	void ratio
T	granular temperature
ρ_p	grain density
d	grain diameter
E_p	grain stiffness
μ_p	interparticle friction coefficient
ε_n	restitution coefficient
$F_{i=1,4}, f_r, \tilde{f}_{i=1,4}$	functions governing collisional response

Γ^{col}	rate of dissipated energy due to particle collsions
$E_f, E_{f,el}, E_{f,k}$	total, kinetic and elastic fluctuating energy
$e_{cc}, e_{ce}, e_c,$	jamming void ratio for compression, extension and general stress state
α_σ	Lode angle
$\dot{\Lambda}$	plastic multiplier
$\boldsymbol{n}$	second order tensors governing plastic strain direction
H	hardening modulus
r	$= \boldsymbol{\sigma}^{qs} : \boldsymbol{\chi},$
$\boldsymbol{s}^{qs*}$	$= \boldsymbol{\sigma}^{qs} - r\chi,$
$J^*_{2\sigma}$	$= 3\boldsymbol{s}^{qs*} : \frac{\boldsymbol{s}^{qs*}}{r^2}$
$J^*_{3\sigma}$	$= 9\sqrt{3}\ \det(\boldsymbol{s}^{qs*})/\boldsymbol{r}^3$
γ, β	parameters governing yield function
$\boldsymbol{s}^{qs}$	$= \boldsymbol{\sigma}^{qs} - \frac{1}{3} I^{qs}_{1\sigma} \boldsymbol{I}$
$\boldsymbol{q}$	hardening variables vector
$\boldsymbol{\chi}$	back stress tensor
F_d	function governing the dilatancy of the material
Ψ, Φ	functions governing function F_d
M_{cs}	limit obliquity at critical state function
$\dot{k}$	$= c_p(\Psi)\sqrt{\dot{\boldsymbol{\varepsilon}}^p : \dot{\boldsymbol{\varepsilon}}^p}$
$\hat{\boldsymbol{\chi}}$	limit tensor of back stress orientation
$\hat{\theta}$	limit rotation angle of back stress orientation
$\boldsymbol{d}$	$= \sqrt{3}\frac{\boldsymbol{s}^{qs*}}{r} - \left(\frac{\sqrt{3}}{3}\frac{\boldsymbol{s}^{qs*}}{r} : \boldsymbol{I}\right)\boldsymbol{I}$
r_c	yield locus cap size
ξ	weight function governing $\dot{r}_c$
$\hat{\xi}$	limit value of ξ at critical state
$I_{1\sigma}$	$= \sigma_x + \sigma_y + \sigma_z$
J_s	$= \left[\frac{1}{3}\left[(\sigma_x - \sigma_y)^2 + (\sigma_x - \sigma_z)^2 + (\sigma_y - \sigma_z)^2\right]\right]^{1/2}$
J_e	$= \left[\frac{1}{3}\left[(\varepsilon_x - \varepsilon_y)^2 + (\varepsilon_x - \varepsilon_z)^2 + (\varepsilon_y - \varepsilon_z)^2\right]\right]^{1/2}$
E, ν	elastic material stiffness parameters
δ_1 and δ_2	flow rule parameters
$\theta_{cc}, \theta_{ec}, \theta_\psi, c_{pc}$ and $c_{p\psi}$	parameters governing $\dot{\boldsymbol{\chi}}$
B_p and ξ_ψ	are parameters governing the isotropic hardening
$\hat{\boldsymbol{F}}$	the fabric tensor calculated from DEM code data

ACKNOWLEDGMENT

This work has been supported by Fondazione Cariplo, Grant no. 2016-0769.

Open Access Funding provided by Politecnico di Milano within the CRUI-CARE Agreement.

DATA AVAILABILITY STATEMENT

Data sharing is not applicable to this article as no new data were created or analysed in this study.

REFERENCES

1. Calvetti F, Emeriault F. Interparticle forces distribution in granular materials: link with the macroscopic behaviour. *Mech Cohesive Frict Mater*. 1999;4(3):247-279.
2. Satake M. Fabric tensor in granular materials. Paper presented at: IUTAM Symposium on Deformation and Failure of Granular Materials (63–68); Delft; 1982.
3. Muir Wood D. The magic of sands—the 20th Bjerrum Lecture presented in Oslo, 25 November 2005. *Can Geotech J*. 2007;44(11):1329-1350.
4. Jop P, Forterre Y, Pouliquen O. A constitutive law for dense granular flows. *Nature*. 2006;441(7094):727-730.

5. Calvetti F, di Prisco C, Redaelli I, Sganzerla A, Vairaktaris E. Mechanical interpretation of dry granular masses impacting on rigid obstacles. *Acta Geotech*. 2019;14(5):1289-1305.
6. Yamamuro JA, Abrantes AE, Lade PV. Effect of strain rate on the stress-strain behavior of sand. *J Geotech Geoenviron Eng*. 2011;137(12):1169-1178.
7. Chialvo S, Sundaresan S. A modified kinetic theory for frictional granular flows in dense and dilute regimes. *Phys Fluids*. 2013;25(7):070603.
8. Sun J, Sundaresan S. A constitutive model with microstructure evolution for flow of rate-independent granular materials. *J Fluid Mech*. 2011;682:590-616.
9. Nicot F, Xiong H, Wautier A, Lerbet J, Darve F. Force chain collapse as grain column buckling in granular materials. *Granul Matter*. 2017;19:18.
10. Tengattini A, Lenoir N, Andò E, Viggiani C. Neutron imaging for geomechanics: a review. *Geomech Energy Environ*. 2021;27:100206.
11. Wiebicke M, Andò E, Viggiani G, Herle I. Measuring the evolution of contact fabric in shear bands with X-ray tomography. *Acta Geotech*. 2020;15(1):79-93.
12. Liu J, Wautier A, Bonelli S, Nicot F, Darve F. Macroscopic softening in granular materials from a mesoscale perspective. *Int J Solids Struct*. 2020;193-194:222-238.
13. Soga K, O'Sullivan C. Modeling of geomaterials behavior. *Soils Found*. 2010;50(6):861-875.
14. Thornton C. Numerical simulations of deviatoric shear deformation of granular media. *Géotechnique*. 2000;50(1):43-53.
15. Baumgarten A, Kamrin K. A general fluid–sediment mixture model and constitutive theory validated in many flow regimes. *J Fluid Mech*. 2019;861:721-764.
16. Alaei E, Marks B, Einav I. A hydrodynamic-plastic formulation for modelling sand using a minimal set of parameters. *J Mech Phys Solids*. 2021;151:104388.
17. Guo X, Peng C, Wu W. Unified constitutive model for granular–fluid mixture in quasi-static and dense flow regimes. *Acta Geotech*. 2021;16:775-787.
18. Dafalias YF, Manzari MT. Simple plasticity sand model accounting for fabric change effects. *J Eng Mech*. 2004;130(6):622-634.
19. Gajo A, Muir Wood D. A kinematic hardening constitutive model for sands: the multiaxial formulation. *Int J Numer Anal Methods Geomech*. 1999;23(9):925-965.
20. Dafalias YF. The concept and application of the bounding surface in plasticity theory. In: Hult J, Lemaitre J, eds. *Physical Non-Linearities in Structural Analysis, International Union of Theoretical and Applied Mechanics*. Springer; 1981.
21. Kolymbas D, Herle I, von Wolffersdorff PA. Hypoplastic constitutive equation with internal variables. *Int J Numer Anal Methods Geomech*. 1995;19(6):415-436.
22. Mašín D. Hypoplastic model for sand. In: *Modelling of Soil Behaviour with Hypoplasticity, Springer Series in Geomechanics and Geoengineering*. Springer; 2019.
23. Darve F. Incrementally non-linear constitutive relationships. In: Darve F, ed. *Geomaterials, Constitutive Equations and Modelling*. Elsevier Science Publisher LTD; 1990:213-238.
24. Bagnold RA. Experiments on a gravity-free dispersion of large solid spheres in a Newtonian fluid under shear. *Proc R Soc Lond Ser A Math Phys Sci*. 1954;225(1160):49-63.
25. Bingham EC. *An Investigation of the Laws of Plastic Flow (No. 278)*. US Government Printing Office; 1917.
26. MiDi GDR. On dense granular flows. *Eur Phys J E*. 2004;14(4):341-365.
27. Redaelli I, di Prisco C. Three dimensional steady-state locus for dry monodisperse granular materials: dEM numerical results and theoretical modelling. *Int J Numer Anal Methods Geomech*. 2019;43(16):2525-2550.
28. Redaelli I, di Prisco C. DEM numerical tests on dry granular specimens: the role of strain rate under evolving/unsteady conditions. *Granul Matter*. 2021;23(2):1-34.
29. Marveggio P, Redaelli I, di Prisco C. A new constitutive approach for simulating solid- to fluid-like phase transition in dry and saturated granular media. In: Barla M, Di Donna A, Sterpi D, eds. *Challenges and Innovations in Geomechanics*. IACMAG 2021. Lecture Notes in Civil Engineering, vol. 125. Springer, Cham; 2021. https://doi.org/10.1007/978-3-030-64514-4_48
30. Berzi D, Di Prisco CG, Vescovi D. Constitutive relations for steady, dense granular flows. *Phys Rev E*. 2011;84(3):031301.
31. Vescovi D, di Prisco C, Berzi D. From solid to granular gases: the steady state for granular materials. *Int J Numer Anal Methods Geomech*. 2013;37(13):2937-2951.
32. Schofield AN, Wroth P. *Critical State Soil Mechanics*. McGraw-Hill; 1968.
33. Campbell CS. Rapid granular flows. *Annu Rev Fluid Mech*. 1990;22(1):57-90.
34. Garzó V, Dufty JW. Dense fluid transport for inelastic hard spheres. *Phys Rev E*. 1999;59(5):5895-5911.
35. Jenkins JT, Savage SB. Theory for the rapid flow of identical, smooth, nearly elastic, spherical particles. *J Fluid Mech*. 1983;130(1):187-202.
36. Lun CKK. Kinetic theory for granular flow of dense, slightly inelastic, slightly rough spheres. *J Fluid Mech*. 1991;233:539-559.
37. Vescovi D, Marveggio P, Di Prisco CG. Saturated granular flows: constitutive modelling under steady simple shear conditions. *Géotechnique*. 2020;70(7):608-620.
38. Redaelli I, Di Prisco C, Vescovi D. A visco-elasto-plastic model for granular materials under simple shear conditions. *Int J Numer Anal Methods Geomech*. 2016;40(1):80-104.
39. Vescovi D, Redaelli I, di Prisco C. Modelling phase transition in granular materials: from discontinuum to continuum. *Int J Solids Struct*. 2020;202:495-510.
40. Jefferies MG. Nor-Sand: a simple critical state model for sand. *Géotechnique*. 1993;43(1):91-103.

41. Huang X, Hanley KJ, O'Sullivan C, Kwok CY, Wadee MA. DEM analysis of the influence of the intermediate stress ratio on the critical-state behaviour of granular materials. *Granul Matter*. 2014;16(5):641-655.
42. Manzari MT, Dafalias YF. A critical state two-surface plasticity model for sands. *Geotechnique*. 1997;47(2):255-272.
43. Berzi D, Jenkins JT. Steady shearing flows of deformable, inelastic spheres. *Soft Matter*. 2015;11(24):4799-4808.
44. Zhao J, Guo N. Unique critical state characteristics in granular media considering fabric anisotropy. *Géotechnique*. 2013;63(8):695-704.
45. Zhou W, Liu J, Ma G, Chang X. Three-dimensional DEM investigation of critical state and dilatancy behaviors of granular materials. *Acta Geotech*. 2017;12(3):527-540.
46. Barreto D, O'Sullivan C. The influence of inter-particle friction and the intermediate stress ratio on soil response under generalised stress conditions. *Granul Matter*. 2012;14(4):505-521.
47. Gajo A, Bigoni D. A model for stress and plastic strain induced nonlinear, hyperelastic anisotropy in soils. *Int J Numer Anal Meth Geomech*. 2008;32:833-861.
48. Golchin A, Lashkari A. A critical state sand model with elastic–plastic coupling. *Int J Solids Struct*. 2014;51(15-16):2807-2825.
49. di Prisco C, Nova R, Lanier J. A mixed isotropic-kinematic hardening constitutive law for sand. *Mod Appr Plast*. 1993:83-124.
50. Been K, Jefferies MG, Hachey J. The critical state of sands. *Geotechnique*. 1991;41(3):365-381.
51. Nova R, Wood DM. A constitutive model for sand in triaxial compression. *Int J Numer Anal Methods Geomech*. 1979;3(3):255-278.
52. Nova R. Sinfonietta classica: an exercise on classical soil modelling. Paper presented at: International Workshop on Constitutive Equations for Granular Non-cohesive Soils (501–519). Cleveland; 1989.
53. Matsuoka H, Nakai T. A new failure criterion for soils in three dimensional stress. Paper presented at: Conference on Deformation and Failure of Granular Materials (253–263), Delft; 1982.
54. Lagioia R, Panteghini A. On the existence of a unique class of yield and failure criteria comprising Tresca, von Mises, Drucker–Prager, Mohr–Coulomb, Galileo–Rankine, Matsuoka–Nakai and Lade–Duncan. *Proc R Soc A: Math Phys Eng Sci*. 2016;472(2185):20150713.
55. Chen YC, Ishibashi I. Dynamic shear modulus and evolution of fabric of granular materials. *Soils Found*. 1990;30(3):1-10.
56. di Prisco C, Imposimato S. Time dependent mechanical behaviour of loose sands. *Mech Cohesive Frict Mater*. 1996;1(1):45-73.
57. di Prisco C, Imposimato S, Aifantis EC. A visco-plastic constitutive model for granular soils modified according to non-local and gradient approaches. *Int J Numer Anal Methods Geomech*. 2002;26(2):121-138.
58. Santucci De Magistris F, Koseki J, Amaya M, Hamaya S, Sato T, Tatsuoka F. A triaxial testing system to evaluate stress-strain behavior of soils for wide range of strain and strain rate. *Geotech Test J*. 1999;22(1):44-60.
59. Vardoulakis I, Aifantis EC. On the role of microstructure in the behavior of soils: effects of higher order gradients and internal inertia. *Mech Mater*. 1994;18(2):151-158.
60. Castro G. *Liquefaction of Sands*. PhD Thesis. Division of Engineering and Applied Physics, Harvard University, Cambridge; 1969.
61. Green PA, Ferguson PAS. On liquefaction phenomena, by Professor A. Casagrande: report of lecture. *Geotechnique*. 1971;21(3):197-202.
62. Hazen A. Hydraulic fill dams. *Trans Am Soc Civil Eng*. 1920;83:1717-1745.
63. Nova R. Controllability of the incremental response of soil specimens subjected to arbitrary loading programmes. *J Mech Behav Mater*. 1994;5(2):193-202.
64. Redaelli I, di Prisco C, Calvetti F. Dry granular masses impacting on rigid obstacles: numerical analysis and theoretical modelling. *Acta Geotech*. 2021;16:3923-3946.
65. Šmilauer V, Catalano E, Chareyre B, et al. Yade reference documentation. *Yade Doc*. 2010;474:1-531.
66. Calvetti F. Discrete modelling of granular materials and geotechnical problems. *Eur J Environ Civil Eng*. 2008;12(7-8):951-965.
67. Babic M. Average balance equations for granular materials. *Int J Eng Sci*. 1997;35(5):523-548.
68. Luding S. Introduction to discrete element methods. *Eur J Environ Civ Eng*. 2008;12:785-826. https://doi.org/10.1080/19648189.2008.9693050
69. Perez JL, Kwok CY, Huang X, Hanley KJ. Assessing the quasi-static conditions for shearing in granular media within the critical state soil mechanics framework. *Soils Found*. 2016;56(1):152-159.
70. Oda M. Fabric tensor for discontinuous geological materials. *Soils Found*. 1982;22(4):96-108.
71. Campbell CS. Granular material flows–an overview. *Powder Technol*. 2006;162(3):208-229.
72. Goldhirsch I. Rapid granular flows. *Annu Rev Fluid Mech*. 2003;35(1):267-293.
73. Jenkins JT. Dense inclined flows of inelastic spheres. *Granul Matter*. 2007;10(1):47-52.
74. Vescovi D. Granular shear flows: constitutive modeling and numerical simulations, PhD thesis, Politecnico di Milano, Milan, Italy. 2014.

How to cite this article: Marveggio P, Redaelli I, di Prisco C. Phase transition in monodisperse granular materials: How to model it by using a strain hardening visco-elastic-plastic constitutive relationship. *Int J Numer Anal Methods Geomech*. 2022;46:2415–2445. https://doi.org/10.1002/nag.3412

APPENDIX A

The DEM numerical campaign consisted in performing constant pressure true-triaxial tests on isotropically consolidated cubical numerical specimens. The 3D open-source software YADE,[65] has been employed. In all analyses, the representative

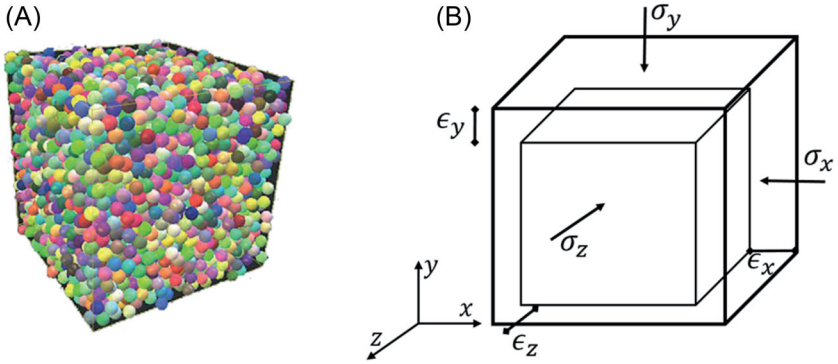

FIGURE A1 RVE: (A) DEM model; (B) reference axis, principal stresses and strains. DEM, discrete element method; RVE, representative volume element

TABLE A1 List of micro-mechanical parameters of the grains

Density ρ_p (kg/m^3)	2600
Diameter d (m)	0.001
Young modulus E_p (MPa)	750
Poisson ratio ν_p	0.17
Friction coefficient μ_p	0.35
Coefficient of restitution ε_n	0.9

elementary volume (REV) is a cubical assembly of $N_p = 5000$ identical particles of diameter d and density ρ_p (Figure A1), free of rotating. In Figure A1, the cubical element with the reference axis is sketched, being σ_x/ε_x, σ_y/ε_y and σ_z/ε_z the corresponding maximum, intermediate and minimum, respectively, principal stresses/strains.

The contact force $\boldsymbol{F}$ is computed by employing a linear visco-elastic model along the normal direction and a liner model set in series with a frictional slider obeying the Coulomb law, along the tangential direction.

The contact law is thus defined once the normal and shear contact stiffnesses k_n and k_t, respectively, the viscous normal coefficient c_n and the interparticle friction coefficient μ_p are assumed. These constants can be calculated from particle Young modulus E_p, Poisson ratio ν_p, restitution coefficient ε_n, diameter d and density ρ_p as is described in Redaelli and di Prisco.[27,28] The micro-mechanical parameters adopted in the numerical simulations coincide with those employed in Redaelli and di Prisco[27,28] and are representative for quartz grains (Table A1).

As in Redaelli and di Prisco.[27,28] to prevent boundaries effects and to apply a homogeneous strain field, periodic boundary conditions have been imposed.

A.1 | Specimens preparation

The numerical specimens are generated by employing the following standard procedure[66]:

I. N_p non-contacting spherical particles are randomly generated in a sufficiently large periodic cubic cell.
II. The system is isotropically compressed by imposing sufficiently low strain rates until a small pressure value ($I_{1\sigma} = \sigma_x + \sigma_y + \sigma_z = 15$ kPa) is got. A time period is waited for long enough to reach static conditions (i.e., unbalanced forces are lower than 1e-5).
During this stage, an interparticle friction coefficient μ_p, ranging between 0 and 0.35, is assigned. The smaller the friction coefficient, the denser the specimen. Three specimens characterised by two different initial void ratios (0.727, 0.657), have been generated by imposing μ_p (II) = 0.1 and 0.3, respectively.
III. μ_p is set equal to 0.35 (see Table 1) and the isotropic compression is continued under quasi-static conditions, by imposing a very small strain rate ($\dot{\varepsilon}_x = \dot{\varepsilon}_y = \dot{\varepsilon}_z = 10\text{e-}3$ s^{-1}) until the desired final value of pressure $I_{1\sigma} = 150$ kPa is achieved.

A.2 | Triaxial loading paths

To simulate heating and cooling described in Section 5, the following servo-control algorithm is applied.

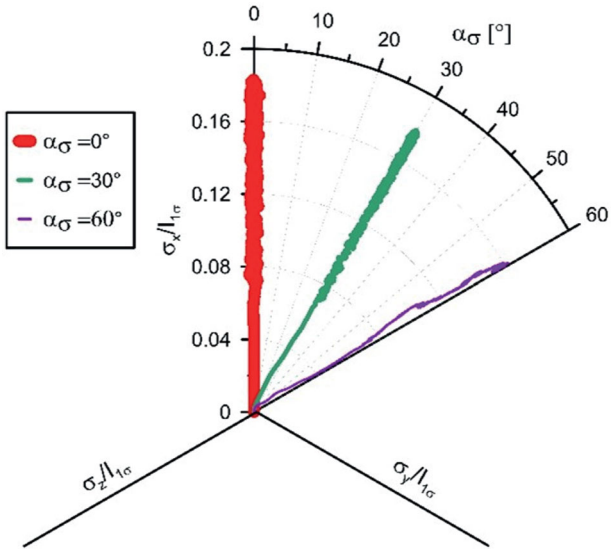

FIGURE A2 Stress paths in the deviatoric plane

The isotropically compressed DEM specimen is deformed under true triaxial conditions by assigning at each time step, the strain rate tensor:

$$\dot{\varepsilon}^t = \begin{bmatrix} \dot{\varepsilon}_x^t & 0 & 0 \\ 0 & \dot{\varepsilon}_y^t & 0 \\ 0 & 0 & \dot{\varepsilon}_z^t \end{bmatrix}.$$

During the true triaxial tests, both pressure $I_{1\sigma}$ and intermediate stress ratio b_σ (or stress Lode angle α_σ) are kept constant during the simulation by adjusting at each time step $\dot{\varepsilon}_y^t$ and $\dot{\varepsilon}_z^t$ as it follows:

$$\dot{\varepsilon}_y^t = \dot{\varepsilon}_y^{t-\Delta t} + g\left(\sigma_y^{req} - \sigma_y^t\right)$$

and

$$\dot{\varepsilon}_z^t = \dot{\varepsilon}_z^{t-\Delta t} + g\left(\sigma_z^{req} - \sigma_z^t\right),$$

where

- σ_y^t and σ_z^t are the current calculated value of the stress along the y- and z-direction, respectively;
- σ_y^{req} and σ_z^{req} are the required values for σ_y and σ_z, respectively, equal to

$$\sigma_y^{req} = b_\sigma\, \sigma_x^t + \frac{1-b_\sigma}{2-b_\sigma}[I_{1\sigma} - \sigma_x^t(1+b_\sigma)],\ \sigma_z^{req} = \frac{I_{1\sigma} - \sigma_x^t(1+b_\sigma)}{2-b_\sigma};$$

- g is a positive gain parameter, evaluated by trial and error, controlling the speed of convergence of the calculated stresses σ_y^t and σ_z^t to the required stress σ_y^{req} and σ_z^{req}.

$\dot{\varepsilon}_x^t$ is calculated by imposing the deviatoric strain rate $\dot{J}_e$:

$$\dot{\varepsilon}_x^t = \frac{1}{2}\left(\dot{\varepsilon}_y^t + \dot{\varepsilon}_z^t\right) - \frac{\sqrt{3}}{2}\left(2\dot{J}_e^2 - \dot{\varepsilon}_y^{t\,2} - \dot{\varepsilon}_z^{t\,2} + 2\dot{\varepsilon}_y^t\dot{\varepsilon}_z^t\right)^{\frac{1}{2}}.$$

In Figure A2, the stress paths in the deviatoric stress plane are shown for $\alpha_\sigma = 0°, 30°$ and $60°$(corresponding to $b_\sigma = 0, 0.5$ and 1, respectively).

The DEM tests described in the paper are listed in Table A2 and are identified by the acronym 'D_X_ $\dot{J}_{e0} - \dot{J}_{ef}$_i', where X

TABLE A2 List of DEM numerical simulations

Test name	e_0	α_σ	$\dot{J}_{e,0,h}$ (s^{-1})	$\dot{J}_{ef}$ (s^{-1})	$\hat{\dot{J}}_e$ (s^{-2})
D_H_0-10_1	0.727	0	0	10	1e6
D_H_0-100_2	0.727	0	0	100	1e6
D_H_0-1_3	0.697	0	0	10	1e6
D_H_0-10_4	0.657	0	0	10	1e6
D_H_0-10_5	0.727	30	0	10	1e6
D_H_0-10_6	0.727	60	0	10	1e6
D_C_10-0_7	0.685	0	10	10	1e6
D_C_100-0_8	0.698	0	100	100	1e6
D_C_100-0_9	0.698	0	100	100	1e5

denotes the test type (H for heating and C for cooling), $\dot{J}_{e0} - \dot{J}_{ef}$ indicates the deviatoric strain rate history and i represents an identification number.

A.3 | Macroscopic quantities

To interpret the DEM response from a macroscopic point of view, the following averaged quantities have been monitored during the tests:

(1) the current logarithmic strain tensor $\boldsymbol{\varepsilon}$ given by:

$$\boldsymbol{\varepsilon} = \log \sum_{i=1}^{t/\Delta t} \dot{\boldsymbol{\varepsilon}}^{i\Delta t} \Delta t \ ,$$

where t denotes the current time instant and Δt is the timestep employed in the explicit integration of the particle law of motion.

(2) the stress tensor, calculated as follows[67,68]:

$$\boldsymbol{\sigma} = \frac{1}{V} \left[\sum_{i=1}^{N_c} \mathbf{F}_i \otimes \mathbf{d}_i + m \sum_{i=1}^{N_p} \mathbf{V}_i' \otimes \mathbf{V}_i' \right],$$

where N_c is the number of contacts within REV, V the periodic cell volume, $m = \rho_d \ \pi d^3/6$ is the particle mass, $\mathbf{d}_i$ the vector joining the centres of two contacting particles and $\mathbf{V}_i'$ the particle velocity fluctuation.
The first term represents the contribution deriving from contact forces, while the second term is the inertial effect associated with particle streaming. This latter is negligible under quasi-static conditions, when inertial forces are largely smaller than contact forces.[8,68]

(3) the void ratio e defined as

$$e = \frac{V_v}{V_s} \ ,$$

where V_s is the volume of the solid fraction and V_v the current volume of voids.

(4) the coordination number Z, measuring the average number of contacts per particles

$$Z = \frac{2N_c}{N_p}$$

(5) the fabric tensor $\hat{\boldsymbol{F}}$ according to Oda[70] and Satake,[2] calculated as it follows:

$$\hat{\boldsymbol{F}} = \frac{1}{N_c} \sum_{i}^{N_c} \mathbf{n}_i \otimes \mathbf{n}_i,$$

being $\mathbf{n}_i$ the unit contact normal vector pointing from centre to centre of two spherical particles in contact.

(6) the internal stored energy E_{stor}, defined as the sum of the elastic strain energy E_{el} and the fluctuating kinetic energy E_{kf}38:

$$E_{stor} = E_{el} + E_{kf}.$$

(7) the elastic stored energy, that is the strain energy stored at all contacts:

$$E_{el} = \frac{1}{2}\sum_{i}^{N_c}\left(\frac{\left|\mathbf{F}_i^n\right|^2}{k_n} + \frac{\left|\mathbf{F}_i^s\right|^2}{k_s}\right),$$

being $\boldsymbol{F}^n$ and $\boldsymbol{F}^s$ the normal and tangential components of the contact force, respectively.

(8) the kinetic fluctuating energy, associated with grain agitation, given by:

$$E_{kf} = \frac{3}{2}\frac{\rho_p}{(1+e)}T,$$

being T the granular temperature, calculated as[33,70,72]):

$$T = \frac{1}{3}\frac{1}{N_p}\sum_{i}^{N_p}\mathbf{V}_i'\cdot\mathbf{V}_i',$$

where symbol · stands for scalar product.

APPENDIX B

Functions $f_i$and $\tilde{f}_i$ appearing in Equation (11) are here defined according to Garzo and Dufty,[34] Berzi and Jenkins,[43,74] and Redaelli et al[27]:

$$f_1 = 4\frac{GF}{1+e}$$

$$f_2 = \frac{4}{3\pi^{1/2}}\frac{QG}{1+e}$$

$$f_3 = \frac{8}{5\pi^{1/2}}\frac{JG}{(1+e)}$$

$$f_4 = \frac{12G}{\pi^{1/2}}\frac{\left(1-\varepsilon_r^2\right)}{(1+e)}$$

$$\tilde{f}_i = f_i\frac{5}{24}\frac{\pi^{1/2}}{G}E_p^{1/2}$$

where

$$G\ (e) = \frac{g_0\,(e)}{1+e}$$

$$g_0\ (e) = q\,(e)\frac{(2e+1)(1+e)^2}{2e^3} + [1-q\,(e)]\frac{2(1+e_c)(1+e)}{e-e_c}$$

$$q\ (e) = \begin{cases} 1 & \text{if } e \geq e_m \\ \dfrac{(1+e_m)\left[(1+e_m)(1+e_c)^2 - 2(1+e)(1+e_c)^2 + (1+e)^2(1+2e_c-e_m)\right]}{(1+e)^2\left[2(1+e_c)(1+e_m) - (1+e_c)^2 + (1+e_m)^2\right]} & \text{if } e < e_m \end{cases}.$$

$$F\ (e) = \frac{1+\varepsilon_n}{2} + \frac{1}{4G\,(e)}$$

$$J\ (e) = \frac{25\pi}{768}\ \frac{(1+e)\,\eta^*\,(e)}{G\,(e)}$$

$$Q\ (e) = \frac{5\pi}{128}\ \frac{(1+e)\,\Gamma^*\,(e)}{G\,(e)}$$

$$\eta^*\ (e) = \left(1 + \frac{4}{5}\,(1+\varepsilon_n)\,G\,(e)\right)\ \eta_k^*\,(e) + \frac{3}{5}\Gamma^*\,(e)$$

$$\Gamma^*\ (e) = \frac{128\pi}{5}\ (1+\varepsilon_n)\left(1 - \frac{1}{32}c^*\right)\frac{g_0\,(e)}{1+e}$$

$$\eta_k^*\ (e) = \left[\left(1 - \frac{1}{4}(1-\varepsilon_n)^2\right)\left(1 - \frac{1}{64}c^*\right)g_0\,(e) - \frac{5}{24}\left(1-\varepsilon_n{}^2\right)\left(1 + \frac{3}{32}c^*\right)g_0\,(e)\right]^{-1}\ \left[1 - \frac{2}{5}\,(1+\varepsilon_n)(1-3\varepsilon_n)\,\frac{g_0\,(e)}{1+e}\right]$$

$$c^* = 32\,(1-\varepsilon_n)\left(1-\varepsilon_n^2\right)\left[81 - 17\varepsilon_n + 30\varepsilon_n^2\,(1-\varepsilon_n)\right]^{-1}$$

$$\varepsilon_r = \varepsilon_n\ - \mu_p \varepsilon_n^{-3/2\,\mu_p}$$

The correlation length L is calculated by employing the formula proposed by Redaelli and di Prisco[27] and depends on void ratio, granular temperature, and anisotropy of the stress tensor:

$$L = \max\left\{d, \frac{d^2 g_1\,(e)\,g_2\,(\alpha_\sigma)\,\dot{J}_e}{T^{1/2}}\right\}\ ,$$

where $g_1(e)$ is a function of the void ratio

$$g_1\ (e) = \left(\frac{4J}{15\left(1-\varepsilon_r^2\right)}\right)^{1/2}\ \left[\frac{2\,(1-\varepsilon_n)}{15}\left(\tilde{g}_0 - \tilde{g}_{0,f}\right) + 1\right]^{3/2},$$

and $g_2(\alpha_\sigma)$ is a function of the Lode angle

$$g_2\ (\alpha_\sigma) = \frac{36}{25}\ \frac{\sqrt{6}}{\sqrt{\pi^3}}\ \frac{J^2(e_c(\alpha_\sigma))}{F^3(e_c(\alpha_\sigma))g_1(e_c(\alpha_\sigma))}\ \frac{1-\varepsilon_r^2}{M_{cs}^3(\alpha_\sigma)}.$$

$\tilde{g}_0$ is a function of the void ratio, reported in Table 3 , and $\tilde{g}_{0,f}$ is the value of $\tilde{g}_0$ at the freezing point ($e = e_f = 1.04$, i.e., the highest value of the void ratio for which correlated motion under simple shear conditions is possible). $\tilde{g}_0$ depends on the parameter $e_m$and the random close packing void ratio $e_{rcp} = 0.57$ (representing the void ratio of the densest possible packing of randomly distributed monodisperse spheres):

$$\tilde{g}_0\ (e) = \tilde{q}\ (e)\ \frac{(2e+1)\,(1+e)^2}{2e^3} + [1 - \tilde{q}\,(e)]\ \frac{2\left(1+e_{rcp}\right)(1+e)}{e - e_{rcp}}$$

$$\tilde{q}\ (e) = \begin{cases} 1 & \text{if } e \geq e_m \\ \dfrac{(1+e_m)\left[(1+e_m)\left(1+e_{rcp}\right)^2 - 2\,(1+e)\left(1+e_{ecp}\right)^2 + (1+e)^2\left(1+2e_{rcp} - e_m\right)\right]}{(1+e)^2\left[2\left(1+e_{rcp}\right)(1+e_m) - \left(1+e_{rcp}\right)^2 + (1+e_m)^2\right]} & \text{if } e < e_m \end{cases}.$$

The ratio between collision time and flight time $f_r(T,e)$, appearing in Equation (11) is defined as:

$$f_r\ (T,e) = 1 + \frac{5}{24}\frac{\pi^{1/2}}{G}\sqrt{\frac{E_p}{\rho_p T}}$$